Bioactive Materials 39 (2024) 375–391

Contents lists available at ScienceDirect

Bioactive Materials

journal homepage: www.keaipublishing.com/en/journals/bioactive-materials

3D printing of interferon γ-preconditioned NSC-derived exosomes/collagen/chitosan biological scaffolds for neurological recovery after TBI

Chong Chen [a,d,1], Zhe-Han Chang [a,1], Bin Yao [a,b,c,1], Xiao-Yin Liu [d,e,1], Xiao-Wang Zhang [a], Jun Liang [a], Jing-Jing Wang [d], Shuang-Qing Bao [a], Meng-Meng Chen [a], Ping Zhu [b,c,**], Xiao-Hong Li [a,*]

[a] Academy of Medical Engineering and Translational Medicine, Tianjin University, Tianjin, 300072, China
[b] Guangdong Cardiovascular Institute, Guangdong Provincial People's Hospital (Guangdong Academy of Medical Sciences), Southern Medical University, Guangzhou, Guangdong, 510100, China
[c] Guangdong Provincial Key Laboratory of Pathogenesis, Targeted Prevention and Treatment of Heart Disease, Guangzhou Key Laboratory of Cardiac Pathogenesis and Prevention, Guangzhou, Guangdong, 510100, China
[d] Tianjin Key Laboratory of Neurotrauma Repair, Characteristic Medical Center of People's Armed Police Forces, Tianjin, 300162, China
[e] Department of Neurosurgery, West China Hospital, West China Medical School, Sichuan University, Chengdu, 610041, Sichuan, China

ARTICLE INFO

Keywords:
Exosomes
Traumatic brain injury
Interferon γ
3D printing
Neural reconstruction

ABSTRACT

The reconstruction of neural function and recovery of chronic damage following traumatic brain injury (TBI) remain significant clinical challenges. Exosomes derived from neural stem cells (NSCs) offer various benefits in TBI treatment. Numerous studies confirmed that appropriate preconditioning methods enhanced the targeted efficacy of exosome therapy. Interferon-gamma (IFN-γ) possesses immunomodulatory capabilities and is widely involved in neurological disorders. In this study, IFN-γ was employed for preconditioning NSCs to enhance the efficacy of exosome (IFN-Exo, IE) for TBI. miRNA sequencing revealed the potential of IFN-Exo in promoting neural differentiation and modulating inflammatory responses. Through low-temperature 3D printing, IFN-Exo was combined with collagen/chitosan (3D-CC-IE) to preserve the biological activity of the exosome. The delivery of exosomes via biomaterial scaffolds benefited the retention and therapeutic potential of exosomes, ensuring that they could exert long-term effects at the injury site. The 3D-CC-IE scaffold exhibited excellent biocompatibility and mechanical properties. Subsequently, 3D-CC-IE scaffold significantly improved impaired motor and cognitive functions after TBI in rat. Histological results showed that 3D-CC-IE scaffold markedly facilitated the reconstruction of damaged neural tissue and promoted endogenous neurogenesis. Further mechanistic validation suggested that IFN-Exo alleviated neuroinflammation by modulating the MAPK/mTOR signaling pathway. In summary, the results of this study indicated that 3D-CC-IE scaffold engaged in long-term pathophysiological processes, fostering neural function recovery after TBI, offering a promising regenerative therapy avenue.

1. Introduction

Traumatic brain injury (TBI) is a global health concern, with over 27 million new cases reported annually worldwide [1]. In China, TBI affects more than 18 % of the global TBI patient population [2]. Primary TBI disrupts the blood-brain barrier (BBB), causing neuronal and neuroglial tissue damage, localized inflammation, and secondary neurodegeneration [3,4]. Vascular damage, long-term neuroinflammation,

Peer review under responsibility of KeAi Communications Co., Ltd.
* Corresponding author.
** Corresponding author. Guangdong Cardiovascular Institute, Guangdong Provincial People's Hospital (Guangdong Academy of Medical Sciences), Southern Medical University, Guangzhou, Guangdong, 510100, China.
E-mail addresses: calphen_cc_gz@163.com (C. Chen), zhchang@tju.edu.cn (Z.-H. Chang), hongyaobin_1212@tju.edu.cn (B. Yao), liuxiaoyin20201110@outlook.com (X.-Y. Liu), 844693629@qq.com (X.-W. Zhang), 15122878711@163.com (J. Liang), dorothyjingjing@163.com (J.-J. Wang), shuangqingbao@163.com (S.-Q. Bao), 19966547251@163.com (M.-M. Chen), tanganqier@163.com (P. Zhu), xhli18@tju.edu.cn (X.-H. Li).
[1] These authors contributed equally to this work.

https://doi.org/10.1016/j.bioactmat.2024.05.026
Received 14 March 2024; Received in revised form 13 May 2024; Accepted 13 May 2024

and neuronal loss collectively hinder TBI self-recovery [5,6]. Therefore, the key to functional recovery after TBI lies in promoting neural regeneration and creating an appropriate microenvironment [7–9]. Despite significant progress in TBI research, effective prevention, treatment, and long-term rehabilitation strategies remain challenging.

Numerous studies have emphasized the potential of exosome-based approaches derived from stem cells in the treatment of TBI [10,11]. In comparison to traditional stem cell therapies, exosome therapy presents several advantages, including low immunogenicity, stable preservation, absence of tumorigenicity, and ethical considerations. Moreover, exosomes retain functions or therapeutic effects similar to their parent cells. Recent advances in stem cell research suggest that neural stem cells (NSCs) release various neurotrophic factors, including brain-derived neurotrophic factor (BDNF), glial cell-derived neurotrophic factor (GDNF), neurotrophin-3 and other paracrine factors [12–14]. Therefore, exosomes derived from NSCs are more suitable for repairing neurological injuries caused by various reasons. NSC-derived exosomes facilitate cell communication and substance transport, both locally and throughout the brain via cerebrospinal fluid [15,16]. They play a vital role in several cellular processes, including immune responses, apoptosis, angiogenesis, and inflammation as well as promote neuroregeneration and recovery of motor function after TBI [17–22]. As the functionality of exosomes is influenced by the cellular microenvironment, an increasing amount of research has been focusing on appropriately adjusting the microenvironment to enhance the targeting efficacy of exosome-based therapies [23–25]. For instance, exosomes derived from plasma subjected to remote ischemic preconditioning have demonstrated efficacy in ameliorating brain ischemia-reperfusion injury [26]. Additionally, exosomes originating from adipose-derived stem cells under hypoxic preconditioning conditions exhibit the ability to enhance angiogenesis and expedite wound healing [27]. Infarct-preconditioning exosomes of umbilical cord mesenchymal stem cells promoted vascular remodeling and neurological recovery after stroke [23]. Therefore, preconditioned NSC-derived exosomes, as a cell-free therapeutic strategy, have the potential to be a highly promising candidate for TBI treatment.

Interferon-gamma (IFN-γ) is a crucial mediator in the inflammatory pathway, playing a key role in neurological diseases [28]. IFN-γ not only supported and initiated post-ischemic brain immune responses but also significantly influenced stem cell differentiation [29–32]. Physiological concentrations of IFN-γ notably enhanced neuronal differentiation *in vitro* [33]. Moreover, further research indicated that IFN regulates the cell cycle of NSCs by suppressing the expression of SOX2 [34]. Furthermore, IFN-γ protected NSCs from central nervous system (CNS) infection-related damage through immune-related bystander effects [33]. Intriguingly, IFN-γ bound to exosomes via Ifngr1 (IFN-γ receptor 1) and activated Stat1 in target cells, suggesting IFN-γ's involvement in exosomes-mediated intercellular communication [35]. Previous studies have shown that IFN-γ, in combination with NSCs, accelerated behavioral improvements in ischemic rats, enhanced neuronal generation, and increased NSC resistance to oxidative stress [29]. Therefore, NSCs preconditioned with IFN-γ may enhance the therapeutic potential of their secreted exosomes in addressing TBI-related neural injuries. However, it is worth noting that TBI has now been linked to chronic traumatic encephalopathy and chronic neuroinflammation [36]. This rendered simple exosome therapy inadequate for addressing the long-term pathophysiological processes of TBI. Therefore, it was necessary to address the challenges related to the delivery and retention of exosomes at the lesion site to enhance their effectiveness during the long-term treatment of TBI.

In recent years, three-dimensional (3D) printed biomaterial scaffolds have been widely used as a comprehensive tissue engineering strategy for treating various neural tissue injuries [22,37,38]. These scaffolds serve as a 3D matrix that supports tissue ingrowth and act as carriers for bioactive factors [39]. Collagen, a primary component of the natural extracellular matrix (ECM), is favored for constructing biomimetic neural microenvironments due to its specific functional peptide sequences that enhance cell adhesion, growth, and differentiation [40–42]. However, collagen's rapid degradation and low mechanical strength render it unsuitable for TBI scaffolds [43]. Chitosan, known for its biodegradability, low toxicity, and good extensibility, is commonly used to promote neural repair and functional recovery in TBI [24,44]. Chitosan is frequently employed as a scaffold carrier that controls growth factor release and extends their activity [45]. Adding chitosan to collagen can delay collagen degradation and enhance the mechanical strength of the collagen scaffold, making collagen-chitosan (CC) scaffolds ideal for TBI treatment [46,47].

Therefore, we hypothesize that incorporating interferon-γ-preconditioned NSC-derived exosomes into the collagen/chitosan scaffold may enhance its therapeutic efficacy for TBI. To maintain the activity of exosomes and align them with the long-term pathophysiological processes of TBI, we adopted a 3D printing technology based on low-temperature extrusion. IFN-γ preconditioned exosomes were uniformly integrated into CC scaffolds. This allowed for controlled release of exosomes, enabling their long-term action at the lesion site and more effectively promoting the reconstruction of neural networks following TBI.

2. Methods

2.1. Animal care and ethical approval

All animal procedures involving animals were conducted in accordance with the approved protocol for the care and use of laboratory animals by the Animal Care Committee of Tianjin University (Ethical approval number: 23658/42, Animal license number: SYXK (Jin) 2021-0003). All SD rats were 8 weeks old and weighed between 240 and 280 g (SPF Biotechnology Co., Ltd., Beijing, China, RRID: RGD_737805, Beijing, China). They were kept in a 12-h light/dark cycle, given food and drink at will, and only allowed to eat before anesthesia.

2.2. Isolation and culture of neural stem cells

Primary NSCs were isolated from the cortex of embryonic rats, obtained from 14-day pregnant female rats. The collected cells were suspended in complete culture medium (DMEM/F12 basal medium supplemented with 20 ng/mL epidermal growth factor, 20 ng/mL basic fibroblast growth factor, 2 % B27plus, 2 % N2, 1 % penicillin-streptomycin, 2 mM glutamax, and 2 mg/mL heparin sodium) in culture flasks and placed in a 37 °C incubator with 5 % CO_2. The culture medium was changed every 3 days, and passaging was performed at day 7. Single cells were detached from neurospheres using accutase dissociation reagent (Sigma) to generate new neurospheres. NSCs were identified using phase-contrast microscopy, and nestin expression was assessed.

2.3. Isolation and collection of NSC exosomes and IFN-γ preconditioned exosomes

Firstly, we explored the concentration of IFN-γ by subjecting NSCs to 10, 20, and 40 ng/mL. Cell viability and differentiation of NSCs were assessed using the MTT assay and immunofluorescence. Exosomes were isolated from NSCs according to established procedures [23]. Briefly, NSCs were treated with IFN-γ (20 ng/mL) for 24 h and cultured without exosome-depleted serum for 2 days (IFN-Exo). The conditioned medium was collected, and cellular debris was removed by centrifugation and 0.22 μm filtration. The remaining precipitate was pelleted at 10,000 g (for 30 min) and 100,000g (for 70 min) at 4 °C. The pellet was resuspended in sterile PBS. In the control group, exosomes were not treated with IFN-γ (Exo). The isolated exosomes derived from NSCs were stored at −80 °C. The morphology of exosomes was identified using transmission electron microscopy (TEM), and their size was analyzed using a

nanoparticle flow cytometer (NanoFCM, N30E, China). Specific surface markers of exosomes, including CD63, HSP70, and TSG101, were detected using western blotting.

2.4. Exosome miRNA sequencing and data analysis

Exo and IFN-Exo were sequenced on an Illumina HiSeqTM 2500 desktop sequence. sRNA sequencing libraries were prepared using the TruSeq Small RNA Sample Prep Kits (Illumina, USA). Differential expression analysis and target gene enrichment analysis were conducted using ACGT101-miR (v4.2). Gene Ontology (GO) and Kyoto Encyclopedia of Genes and Genomes pathway (KEGG) enrichment analyses were used according to p-value <0.05 of exclusion criteria.

2.5. The impact of IFN-Exo on cultured cells

NSCs were treated with Exo and IFN-Exo, and the differentiation status of NSCs was identified through the expression of DCX and NeuN. Microglial cells (BV2) were seeded in culture flasks containing complete growth medium (DMEM basal medium supplemented with 10 % FBS). Cultured cells with similar density were subjected to simple randomization by QuickCalcs from GraphPad. The experiments were repeated at least three times for each experiment, unless stated otherwise. Lipopolysaccharide (LPS) was utilized to induce an *in vitro* neuroinflammation model. To put it simply, BV2 cells were cultured for 6 h in complete growth medium containing LPS (1 μg/mL). Exo and IFN-Exo were added to the complete growth medium 24 h before LPS induction. Anisomycin (p38MAPK agonist, HY-18982, MCE, USA) was used to investigate the molecular mechanisms. Primary neurons were isolated from the hippocampus of embryonic rats, obtained from 18-day pregnant female rats. Collected cells were cultured in neural maintenance medium (Neurobasal with 2 % B27plus, 1 % penicillin-streptomycin and 0.5 mM glutamax), with medium replacement every 3 days. The oxygen-glucose deprivation/reperfusion (OGD/R) model was employed to simulate the *in vitro* neuronal injury process. In brief, primary neurons were cultured for 12 h in a glucose-free medium with 95 % N_2 and 5 % CO_2 at 37 °C, followed by 24 h of cultivation in complete growth medium under normoxic conditions (21 % O_2). Exo and IFN-Exo were added to the complete growth medium 24 h before the initiation of the OGD/R model. Cells from each group were collected, and the expression of Bax, Bcl-2, IL-1β, IL-6, iNOS, P2Y12 and Arg1 was assessed through Western blotting and qPCR (All primers are shown in Table 1). Cell viability of primary neurons were determined using the MTT technique.

2.6. Traumatic brain injury model

Rats were randomly assigned to four groups: Sham, TBI, 3D-CC-E, and 3D-CC-IE (n = 30 rats for each group). The researchers labeled the rats using ear tags, and the study was conducted in a blinded manner. Blinding was achieved by ensuring that the experimenters were unaware of the animal groupings during both the experimental and statistical analysis phases. Different individuals performed the analysis or experimental grouping using animal codes for blind quantitative analysis.

A previously established method was utilized to create the TBI rat model (68099II, RWD, Shenzhen, China) [24]. Briefly, rats were anesthetized with isoflurane inhalation (3 % for induction and 1.5 % for maintenance (v/v)) to ensure adequate anesthesia throughout. In the right parietal region of the rat skull, a stereotaxic device was used to produce a 5-mm bone window (2.1 mm posterior to the coronal suture and 3.8 mm lateral to the sagittal suture). The rats were then subjected to impact injury using a controlled cortical impact device (parameters: depth 2 mm, impact velocity 5 ms^{-1}, dwell time 12 ms). Wound hemostasis was achieved by local drops of thrombin (50–1000 units/mL) during surgery (Solarbio, Beijing, China), and postoperative intramuscular injection of tramadol (1 mg/kg) (Solarbio, Beijing, China) was used for pain relief. After surgery, rats were placed on a warm pad until they woke up.

Table 1
Primer sequences of each gene.

Target	Forward	Reverse
iNOS	TGAGGATTACTTCTTCCAGCTCA	TGGGTGTCAGAGTCTTGTGC
IL-1β	AGCAGCTTTCGACAGTGAGG	CTCCACGGGCAAGACATAGG
P2Y12	CTCCACCACCTACATGTTTC	AAGAGGATGCTGCAGTAGAG
Arg1	CTACCTGCTGGGAAGGAAG	GTCCTGAAAGTAGCCCTGTC
Bax	GGATACAGACTCCCCCCGAG	AACATGTCAGCTGCCACACG
Bcl-2	CAGAGGGCTACGAGTGG	CAGAGCGATGTTGTCCAC
GAPDH	AGACAGCCGCATCTTCTTGT	CTTGCCGTGGGTAGAGTCAT

2.7. Preparation of 3D-printed IFN-γ preconditioned exosome/collagen/chitosan scaffolds

Collagen/chitosan composite materials were prepared as previously described [24,48]. Briefly, a sterile composite consisting of 6 g of collagen and 3 g of chitosan (deacetylation degree 75–85 %, Sigma, St. Louis, USA) was warmed overnight at 4 °C. The exosome solution was sterilized at 4 °C using a 0.22 μm filter (Millipore, USA). Then to equilibrate the binding, 2 mg/mL of exosomes were mixed in collagen/chitosan solution and after stirring for 12 h at 4 °C, the mixed solution was warmed at 4 °C overnight. Structures were prepared by a 3D printer (Regenovo, China) at −20 °C. The printing parameters were as follows: platform temperature = −20 °C, nozzle diameter = 160 μm, extrusion speed = 0.17 mm/min, printing speed = 12 mm/s, and thickness of each layer = 0.3 mm. The prepared hybrid solution (collagen/chitosan composite or collagen/chitosan composite combined with exosome) was placed into the printer cartridge. After printing, the 3D solid molded parts (3D-printed collagen/chitosan scaffolds (3D-CC)) and 3D-printed collagen/chitosan scaffolds integrated with exosomes (3D-CC-E and 3D-CC-IE)) were stored at −80 °C overnight, and then vacuum-cooled and dried for 72 h 3D-CC-E and 3D-CC-IE were made into cylinders with a diameter of 2 mm and a height of 2 mm using a hole punch. All scaffolds were sterilized with Co-60 at 4 °C and washed with D-Hank's for 30 min.

2.8. Scanning electron microscopy

To prepare the 3D-CC-E and 3D-CC-IE scaffolds for scanning electron microscopy (SEM), they were fixed in 2 % glutaraldehyde and 1 % osmium tetroxide, dehydrated in a graded acetone series. The samples were rapidly frozen to the desired temperature using liquid nitrogen and then lyophilized for 12 h. The dried samples were then coated with gold and examined using a scanning electron microscope (Hitachi, Japan).

2.9. Scaffold characteristics

The water absorption and porosity of the scaffolds were measured using gravimetric and volumetric methods [49]. Tree samples of each dried scaffold were obtained and soaked in 0.01 mol L^{-1} PBS at pH 7.4 for 24 h to reach equilibrium to assess water absorption. The weight of water adsorbed on the surface was noted as m0 and the mass after drying in a desiccator for 2 h was noted as m1. Water absorption was calculated by the following equation: water absorption (%) = (m0-m1)/m1 × 100 %. The porosity of the scaffold was measured using the liquid replacement method with ethanol as the replacement fluid. The mechanical quality of the scissors was evaluated using an Instron 5865 material testing equipment (Instron, USA). After reaching equilibrium, the scissors were immersed in 0.01 M PBS at 37 °C for 24 h. Three sets of samples were then taken to determine the modulus of elasticity in compressive strain. A tree cycle with a 0.5 Hz sawtooth wave was used to apply a preload of 0.1 N in 50 % increments at 100 %/min.

2.10. Determination of exosome release kinetics in 3D-CC-IE

3D-CC-IE was incubated in PBS at 37 °C, and the supernatant was collected at day 0, 2, 4, 6, 8, 10, 12, and 14. After that, the supernatant was totally replaced with new PBS. The BCA protein concentration assay kit was used to count the concentration of exosomes in the supernatants at each time point. The 3D-CC scaffold was also detected as a substrate control to correct the effect of protein degradation in the system.

2.11. Cytocompatibility of scaffolds and cell staining

Exosomes were labeled with DiI red fluorescent membrane-conjugated dye according to the manufacturer's protocol, and phagocytosis of exosomes was assayed by culturing NSCs with 3D-CC-IE scaffolds for 24 h. After staining the cytoskeleton with ActinTracker Green, laser confocal microscopy was used to obtain the morphology of exosomes phagocytosed by cells. 3D-CC-IE was cultured with NSCs for 7 days (each scaffold received 100 μL NSCs at a concentration of 1×10^6/mL). Immunofluorescence staining of the cytoskeleton complexes was performed. The development of NSC on the scaffolds was examined by labeling FDA/PI and F-actin using laser confocal microscopy. MTT technique (Solarbio, Beijing, China) was used to determine the viability of cells on 3D-CC-E and 3D-CC-IE at day 1, 3, 5, and 7 after culture. NSCs were injected onto the scaffolds with 20 μL of single-cell solution at a concentration of 5×10^6/mL. NSCs on the scaffolds were digested using Accutase (Gibco, A1110501, USA) for 5–8 min and resuspended using complete medium, and subsequently cell counting was performed. The cell adhesion rate of NSCs was determined at 1, 12, 24, 36, 48, 60, and 72 h after inoculation using the formula cell adhesion rate = (number of adherent cells/number of inoculated cells) × 100 %.

2.12. Scaffold implantation

Before implantation, cylindrical brain tissue samples (2 mm in diameter and 2 mm in height) were taken using a mold. The cylindrical scaffolds (2 mm in diameter and 2 mm in height) were implanted into the cavity after hemostasis. The wounds were tightly sutured, and then the rats were placed in a warm cage to recover from anesthesia. After TBI surgery, tramadol (1 mg/kg) (Solarbio, YZ-171255, Beijing, China) and penicillin sodium (15 mg/kg) (Solarbio, C8250, Beijing, China) were given to all rats to relieve pain and avoid infection.

2.13. Neurological function assessment

Modified Neurologic Severity Score (mNSS) was performed at day 1, 3, 7, 14, 21, and 28 after TBI to assess neurologic recovery (n = 10 per group). On an 18-point scale, the mNSS received a score. Rats were taught and tested before surgery to verify normal results (0).

From day 21–26 following TBI surgery, the Morris water maze (MWM, XR-XM101-Z, Xinruan, Shanghai, China) test was administered to evaluate cognitive function (n = 10 per group). Prior to training, the platform was positioned in the northeastern quadrant, and the rats were put in the pool facing the wall. The duration needed to jump into the water and ascend the platform was called the escape latency. When the rats found the platform and remained there for at least 2 s, training was deemed successful. The training of the rats was deemed successful if they were unable to locate the hidden platform in 60 s. Rats that failed to find the hidden platform within 60 s were guided to the platform location and their escape latency was recorded as 60 s. Each rat underwent four training sessions. 27 days after TBI, the platform was removed, and the rats underwent a spatial search experiment to test their cognitive abilities. The escape latency, the number of times the platform was traversed, and the time spent in the target quadrant were recorded and analyzed.

2.14. Histological observations

At 2 month after TBI, histological assessments were conducted, including Luxol Fast Blue (LFB) staining, Bielschowsky's silver staining, Nissl staining, HE staining, Golgi's staining and immunofluorescence (n = 5 for each group). Additional, for the *in vivo* biocompatibility of the scaffolds, HE staining of the heart, liver, spleen, lung and kidney of rats after scaffold transplantation was performed. Liver function and renal function of rat were also examined. BrdU was injected for 7 days after completion of 3D-CC-E and 3D-CC-IE scaffolds implantation to label neoplastic cells (n = 3). Rats were anesthetized by intraperitoneal injection of pentobarbital sodium solution at a concentration of 1.3 % (40 mg/kg). Sequential infusions of saline and 4 % paraformaldehyde were given to the heart. Brain tissue sections (30 μm thick) were prepared in the coronal plane. Sections were permeabilized with 0.5 % Triton X-100 and sealed with 10 % normal goat serum (NGS). Primary antibodies were mouse-NF (1:300, Abcam, UK, ab315188), rabbit-MBP (1:300, Abcam, UK, ab218011), rabbit-MAP2 (1:250, Abcam, UK, ab183830), rabbit-GFAP (1:1000, Abcam, UK, ab7260), rabbit-iba1 (1:1000, Abcam, UK, ab178846), rabbit-vWF (1:300, Invitrogen, USA, PA5-80223), mouse-Arginase 1 (1:200, Proteintech, 66129-1-Ig), rabbit-iNOS (1:20, Invitrogen, USA, PA1-036), rabbit-NeuN (1:200, Invitrogen, USA, 702022), rabbit-DCX (1:250, Abcam, UK, ab207175), mouse-nestin (1:100, Invitrogen, USA, 14-5843-82) and mouse-BrdU (1:200, Abcam, UK, ab8152). Sections were incubated with primary antibody overnight at 4 °C and then incubated with matching secondary antibody (Alexa Fluor 488 (Goat anti-Rabbit IgG) or Alexa Fluor 594 (Goat anti-Mouse IgG)) for 1 h at room temperature in the dark. Sections were restained with Hoechst 33342 (H3570, Invitrogen, USA). Stained images at 400 × magnification were selected for quantitative statistics. Quantitative statistical analysis of all stainings were performed by ImageJ software (NIH, USA).

2.15. Transmission electron microscopy

The ultrastructural changes of neurons were examined by transmission electron microscopy (TEM) after TBI. Rats were anesthetized with 1.3 % sodium pentobarbital (40 mg/kg) and injected transcardially with 4 % paraformaldehyde and 2 % glutaraldehyde (n = 5 per group). Injured brain tissue was separated and cut into 1 mm^3 size cubes. Samples were fixed using two percent glutaraldehyde and one percent osmium acid. The brain tissue blocks were then dried and embedded in Epon 812 embedding medium (Solarbio, Beijing, China). A series of sections with thicknesses between 70 and 90 nm were cut using an ultrathin sectioning machine, double-stained with lead and dioxin acetate, and then studied using a JEM 1210 TEM (JEM 1210; JEOL, Tokyo, Japan). Ten random field images were taken for each sample at 5000 × magnification. Quantitative analysis of TEM was performed using ImagePro Plus software (Media Cybernetics, USA).

2.16. Statistical analysis

Statistical analysis was performed using GraphPad Prism 7.0 software (RRID:SCR_002798). Data collection and analysis were conducted by blinded experimenters. One-sample Kolmogorov-Smirnov tests were performed to assess the normality of data in this study. Data are reported as mean ± standard deviation. Statistical significance was determined by one-way analysis of variance (ANOVA) and Bonferroni analysis for multiple comparisons. Two-tailed Student's *t*-test was performed for pairwise comparisons. $P < 0.05$ was considered statistically significant.

3. Results

3.1. Extraction and identification of IFN-Exo

The morphology of NSCs was identified using phase-contrast

microscopy after pre-treatment with interferon-γ (Fig. 1A). To explore the optimal concentration of IFN, 10, 20, and 40 ng/mL of IFN were separately added to the complete culture medium. The differentiation and cell viability of NSCs were assessed. Quantitative analysis revealed a significant increase in the expression of DCX (Figs. S1A and B), NeuN (Figs. S1C and D), and MAP2 (Figs. S1E and F) in the IFN (20) group compared to the IFN (10) group, with no significantly improved effects observed in the IFN (40) group. Cellular viability showed no significant differences among the groups (Fig. S1G). Therefore, we selected 20 ng/mL of IFN as the optimal concentration for NSCs treatment. NSCs were examined using a differential interference microscope (Fig. 1B). Exosomes derived from NSCs were identified via transmission electron microscopy and displayed a double-layered, cup-shaped or elliptical structure (Fig. 1C). The peak particle size of the exosomes pellets was measured at 105 nm for Exo and 113.2 nm for IFN-Exo (Fig. 1E). Western blotting confirmed the positive expression of specific protein markers, including Hsp70, CD63, and TSG101 (Fig. 1D). The concentration of Exo, as evaluated by the BCA method, was seen to be 0.68 mg/mL and 0.79 mg/mL (Fig. 1F). The positive expression of DiI indicated that exosomes (Exo and IFN-Exo) could be engulfed by cells (Fig. 1G). The results suggested that there were no significant differences in the morphology, distribution, and internalization of IFN-Exo compared to Exo.

3.2. IFN-Exo enhanced the differentiation and maturation of NSCs

To determine the mechanism by which IFN-Exo promoted the development of NSCs, we performed miRNA-sequencing. Firstly,

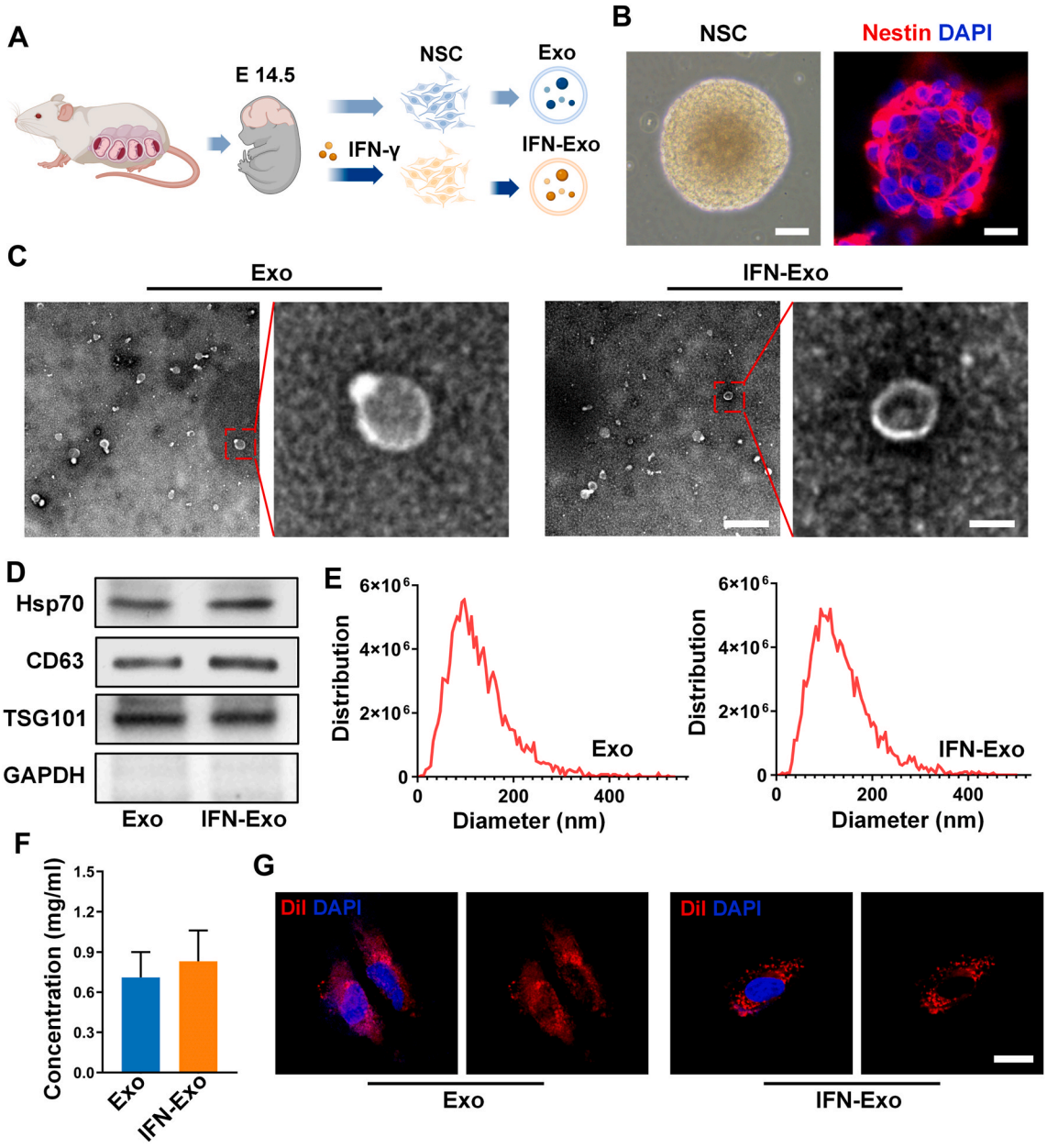

Fig. 1. Characterization of exosomes derived from NSCs and IFN-preconditioned NSCs.
(A) Schematic of Exo and IFN-Exo extraction. (B) Identification of NSC. (C) Morphological characteristics of Exo and IFN-Exo under transmission electron microscopy. (D) Exosomal-specific protein markers HSP70, CD63 and TSG101 investigated by western blotting. (E) Measurement of the diameter of Exo and IFN-Exo. (F) Concentration of Exo and IFN-Exo. (G) Labelling of phagocytosed exosomes by PKH26. Scale bars: 100 μm in (B left), 20 μm in (B right), 1 μm in (C left), 100 nm in (C right), 25 μm in (G).

principal component analysis showed significant differences in the composition between IFN-Exo and Exo (Fig. S2A). The volcano plot indicated 175 significantly upregulated and 447 significantly downregulated miRNAs among the differential miRNAs (Fig. S2B). Gene Ontology (GO) analysis highlighted the significant enrichment of differentially expressed miRNAs in processes related to neural development, such as neuronal cell body, axon, dendrite, glutamatergic synapse, and neuronal projection (Fig. 2A). Kyoto Encyclopedia of Genes and Genomes (KEGG) analysis revealed highly enriched pathways including axon guidance and synaptogenesis (Fig. 2B). Hierarchical clustering heatmaps displayed an upregulation in the expression profile of neural differentiation genes (such as miR-7b, miR-10a, and miR-124-5P) and a downregulation in the expression profile of stem cell genes (such as miR-23b-3p, miR-30a-3p, miR-214-3P) in IFN-Exo group compared to the Exo group (Fig. 2C). These results suggested that IFN-Exo has a promoting effect on NSCs differentiation and maturation. The significant elevation of DCX and NeuN after IFN-Exo preconditioning further supported the findings from the sequencing analysis (Fig. 2D–F).

3.3. IFN-Exo alleviated neuroinflammation induced by LPS

In addition to its role in promoting neural differentiation, we also observed a significant enrichment of inflammatory responses in the results of GO and KEGG analyses, such as responses to LPS and TNF, the PI3K-Akt signaling pathway, the NF-κB signaling pathway, and the TGF-

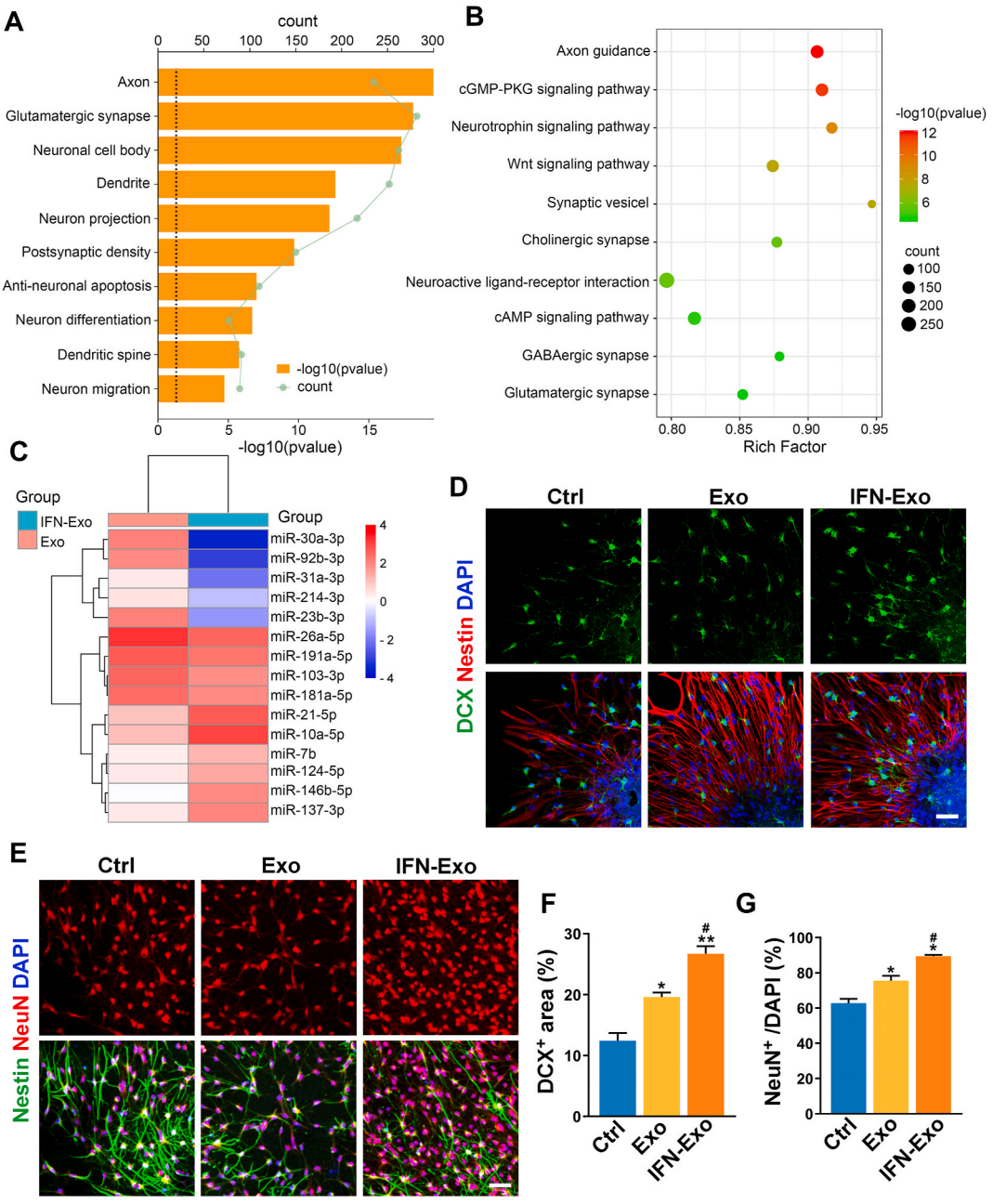

Fig. 2. IFN-Exo promoted NSCs differentiation into neurons.
(A) The top 10 GO functions of predicted targets in neural differentiation. (B) The top 10 KEGG Pathway enrichment analysis of differential expression genes in neural differentiation. (C) Clustered heatmap of differential miRNA expression between IFN-Exo and Exo. (D) Immunofluorescence staining of Nestin/DCX among Ctrl, Exo and IFN-Exo. (E) Immunofluorescence staining of Nestin/NeuN among Ctrl, Exo and IFN-Exo. (F) Statistical calculation of DCX^+ and $NeuN^+$. All data were expressed as mean ± SD; $^*P < 0.05$, $^{**}P < 0.01$ *vs.* Ctrl; $^{\#}P < 0.05$ *vs.* Exo.

β signaling pathway (Fig. 3A and B). The differentially expressed miRNAs revealed by hierarchical clustering heatmap were also significantly associated with inflammatory responses, consistent with published results (Fig. 3C). To investigate this further, we utilized the BV2 microglial cell line to simulate an *in vitro* inflammation model induced by LPS (Fig. S2C). The relative expression levels of selected significantly changed genes (IL-1β, iNOS, P2Y12 and Arg1) were consistent with qPCR verification (Fig. 3D). The IFN-Exo group exhibited a significant downregulation of M1 microglial cell markers IL-1β, IL-6, and iNOS, while M2 markers Arg1 and P2Y12 were significantly upregulated (Fig. 3E and F). These results confirmed that IFN-Exo has an anti-neuroinflammatory effect. Further mechanistic validation suggested that the p38MAPK/mTOR signaling pathway was down-regulated after IFN-Exo treatment and that this effect was reversed by Anisomycin (Figs. S3A–F). The results of Western blotting and qPCR indicated that following OGD/R, primary neurons exhibited increased Bax expression and decreased Bcl-2 expression, suggesting severe neuronal damage (Figs. S2D–F). Treatment with Exo and IFN-Exo alleviated neuronal

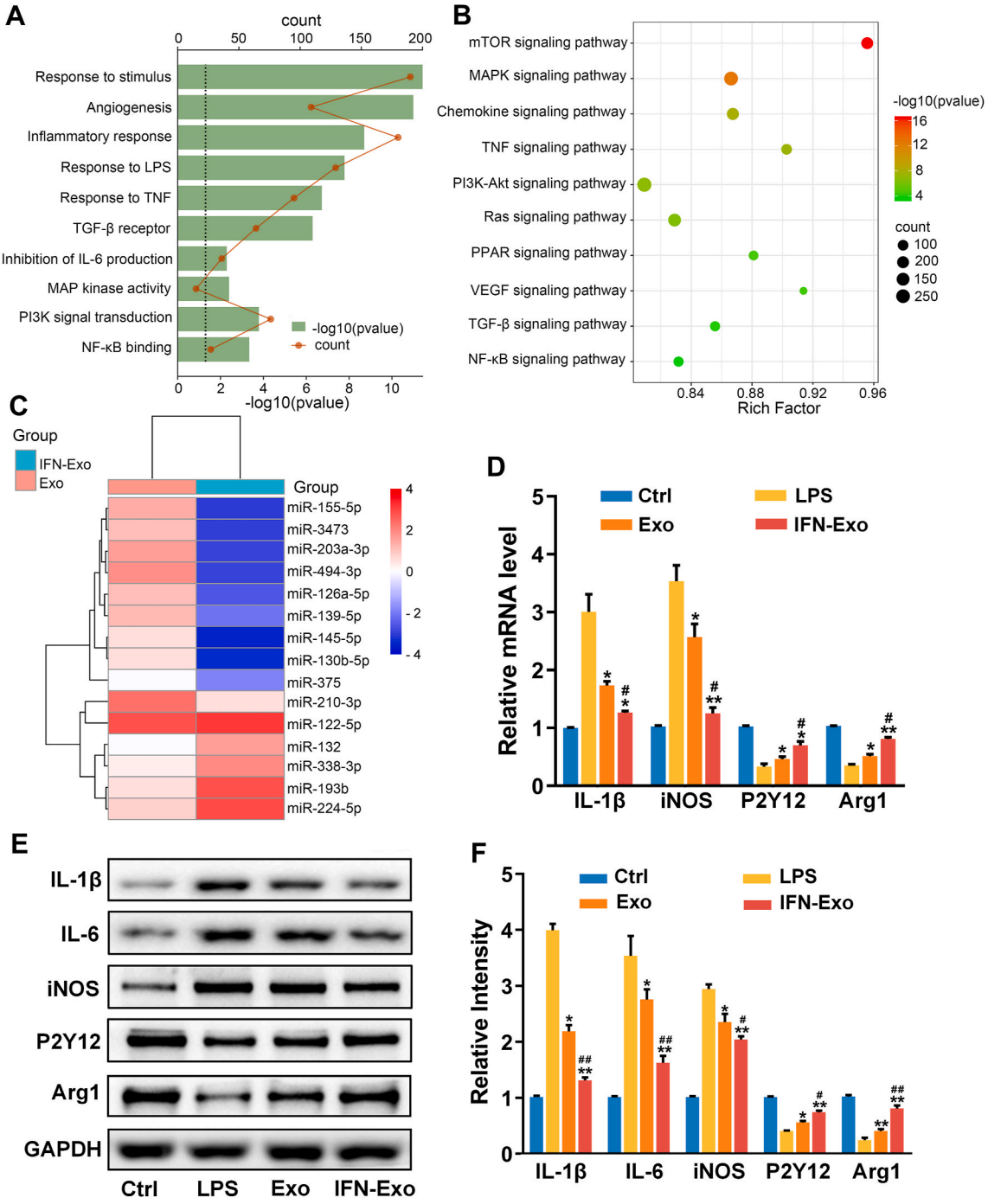

Fig. 3. IFN-Exo reduces neuroinflammation *in vitro*.
(A) The top 10 GO functions of predicted targets in inflammatory reaction. (B) The top 10 KEGG Pathway enrichment analysis of differential expression genes in inflammatory reaction. (C) Clustered heatmap of differential miRNA expression between IFN-Exo and Exo. (D) Relative mRNA (IL-1β, iNOS, P2Y12 and Arg1) level among Ctrl, LPS, Exo and IFN-Exo. (E) IL-1β, IL-6, iNOS, P2Y12 and Arg1 among three groups investigated by western blotting. (F) Statistical calculation of relative protein intensity. All data were expressed as mean ± SD; $^{*}P < 0.05$, $^{**}P < 0.01$ *vs.* LPS; $^{\#}P < 0.05$, $^{\#\#}P < 0.01$ *vs.* Exo.

damage, with the IFN-Exo group demonstrating a more potent therapeutic effect (Figs. S2D–F). Similarly, the significantly increased cell viability in the IFN-Exo group compared to the Exo group revealed that IFN-Exo possessed a more robust neuroprotective effect (Fig. S2G).

3.4. 3D-CC-IE exhibited excellent physical properties and favorable biocompatibility

The 3D-CC-IE was fabricated using a 3D printer (Fig. 4A and B). Electron microscopy and HE staining images showed the porous structure of 3D-CC-IE, providing a favorable environment for cell attachment and proliferation (Fig. 4C–E). NSCs exhibited excellent growth within the 3D-CC-IE scaffold (Fig. 4F). Confocal laser microscopy revealed the presence of peripheral red-labeled exosomes (PKH26) in the nucleus (Fig. S4A), indicated the capability of NSCs to uptake exosomes. Fixed and stained NSCs cultured for 7 days on 3D-CC-E and 3D-CC-IE scaffolds showed increased cell viability, as indicated by the increase in FDA and F-actin staining (Figs. S4B and C). The absorbance of NSCs in the 3D-CC-IE group significantly increased compared to the 3D-CC-E group at day 3, 5, and 7 (Fig. S4D). Moreover, cell adhesion of NSCs in the 3D-CC-IE group was significantly higher than in the 3D-CC-E group during the same period (Fig. S4E). Laser scanning confocal microscopy and electron microscopy images displayed exosomes adhering to the 3D-CC-IE scaffold (Fig. 4G and H). The elastic modulus of 3D-CC-E (41.53 ± 6.373)

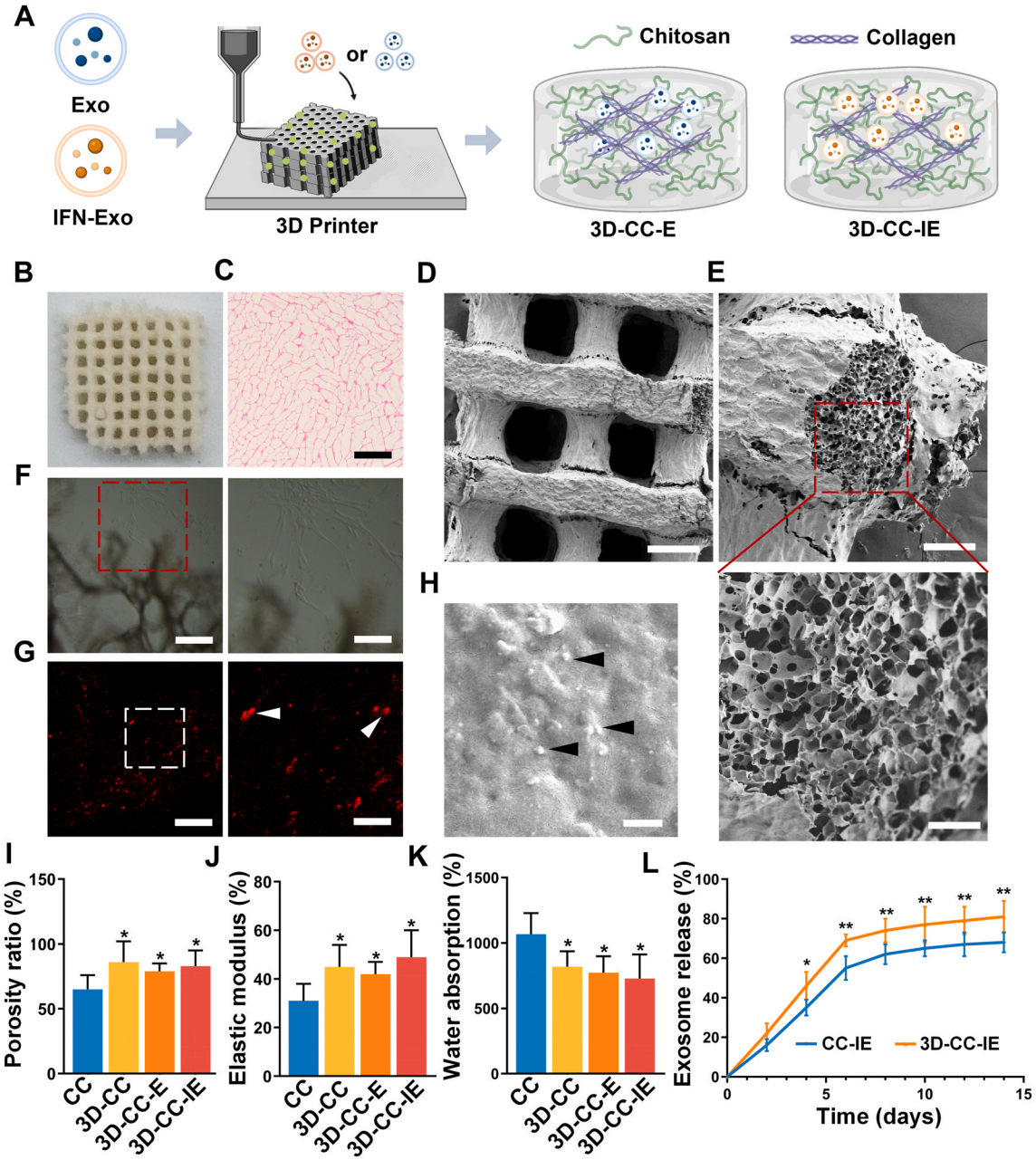

Fig. 4. Characterisation of 3D-CC-IE scaffolds.
(A) Schematic diagram of 3D-CC-E and 3D-CC-IE scaffold preparation. (B–E) Representative images of 3D-CC-IE under general view (B), HE staining (C) and SEM (D and E). (F) Neural stem cells cultured on 3D-CC-IE scaffolds. (G) Representative 3D fluorescent image illustrated the distribution of exosomes within the 3D-CC-IE. (H) The distribution of exosomes within the 3D-CC-IE scaffold. (I–K) The porosity ratio (I), elastic modulus (J), and water absorption (K) of the scaffolds. (L) Cumulative release profile of IFN-Exo from the CC-IE and 3D-CC-IE within 14 days. All data were expressed as mean ± SD; $^{*}P < 0.05$, $^{**}P < 0.01$ *vs.* CC or CC-IE. Scale bars: 50 μm in (C, G and H), 200 μm in (D), 100 μm in (E top), 20 μm in (E bottom), 500 nm in (F).

and 3D-CC-IE (46.17 ± 4.452) was significantly higher than that of CC (32.68 ± 4.252), suggesting enhanced tissue regeneration support (Fig. 4J). The water absorption rate of 3D-CC-IE (780.12 ± 128.317) was lower than CC (1140.08 ± 158.238), confirming that the 3D-printed collagen/chitosan scaffold was conducive to exosomes maintenance (Fig. 4K). Furthermore, 3D-CC-E (85.28 ± 11.178) and 3D-CC-IE (79.45 ± 7.904) exhibited a greater pore size than CC (65.58 ± 8.368), promoting nutrient diffusion (Fig. 4I). From day 1 to day 14, the 3D-CC-IE group showed higher and more stable release than the CC-IE group, ensuring the beneficial effects of exosomes *in vivo* (Fig. 4L). These results demonstrated that the 3D-CC-IE scaffold was more biocompatible. Evidently, this robust effect originated from interferon-γ preconditioned exosomes.

3.5. 3D-CC-IE implantation enhanced neurological function recovery after TBI

We then investigated whether 3D-CC-IE implantation could enhance motor function recovery and repair brain damage (Fig. 5A). One day after TBI, all injured rats showed increased mNSS scores. Compared to the TBI group, the mNSS scores were reduced in the 3D-CC-E and 3D-CC-IE groups (Fig. 5B). Notably, 3D-CC-IE treatment restored neurological function to a higher level than that in 3D-CC-E (Fig. 5B). The Morris water maze test was used to evaluate the cognitive benefits of 3D-CC-IE. Rats subjected to 3D-CC-IE treatment displayed shorter paths after TBI, suggesting a significant improvement in spatial memory (Fig. 5C). Compared to the TBI group, the 3D-CC-E group improved cognitive function by reducing the latency period, increasing time spent in the target quadrant, and the number of platform crossings. Importantly, the 3D-CC-IE group exhibited a shorter latency period, more time spent in the target quadrant, and more platform crossings compared to the 3D-CC-E group (Fig. 5D–F).

3.6. 3D-CC-IE exhibited good biocompatibility in vivo

In order to validate the viability of 3D-CC-IE for TBI treatment, the *in vivo* tolerance to 3D-CC-IE exposure was further investigated. HE staining of vital organs, including the heart, liver, spleen, lungs, and kidneys, at 1 and 2 month after TBI, revealed no overt physiological anomalies as compared to the Sham group (Figs. S5A–B). Additionally, hepatic and renal function indicators following 3D-CC-IE transplantation, such as alanine aminotransferase (ALT), creatinine (CR),

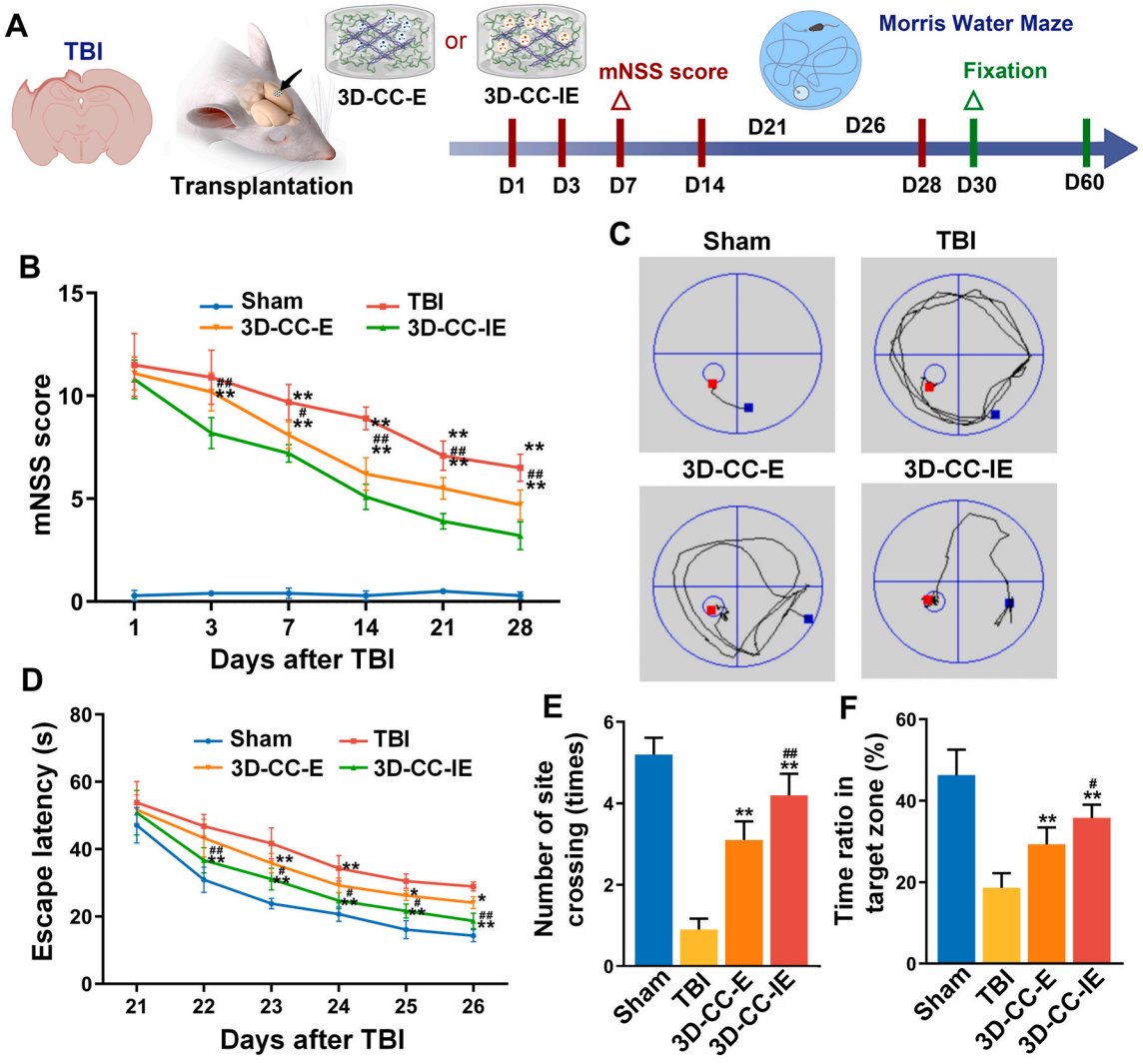

Fig. 5. The characterization of neural functional recovery following TBI in rats.
(A) Schematic of the timing of scaffolds implantation and various tests. (B) The mNSS scores were recorded at 1, 3, 7, 14, 21, and 28 days after implantation of scaffolds after TBI. (C) Representative swimming paths in the Morris water maze among Sham, TBI, 3D-CC-E and 3D-CC-IE. (D–F) Escape latency (D), number of site crossing (E), and time ratio in the target zone (F) among four groups. All data were expressed as mean ± SD; $^{*}P < 0.05$, $^{**}P < 0.01$ *vs.* TBI; $^{\#}P < 0.05$, $^{\#\#}P < 0.01$ *vs.* 3D-CC-E.

aspartate aminotransferase (AST), and blood urea nitrogen (BUN), remained within normal parameters (Figs. S5C–F). These results affirmed the biocompatibility of 3D-CC-IE and its lack of deleterious effects on the organism, rendering it an exemplary choice for TBI therapy.

3.7. 3D-CC-IE implantation enhanced tissue remodeling and mitigates glial scarring

To further assess the efficacy of 3D-CC-IE in TBI treatment, brain tissue sections were subjected to HE staining 2 months after TBI. The overall view of brain tissue showed a significant reduction in the loss

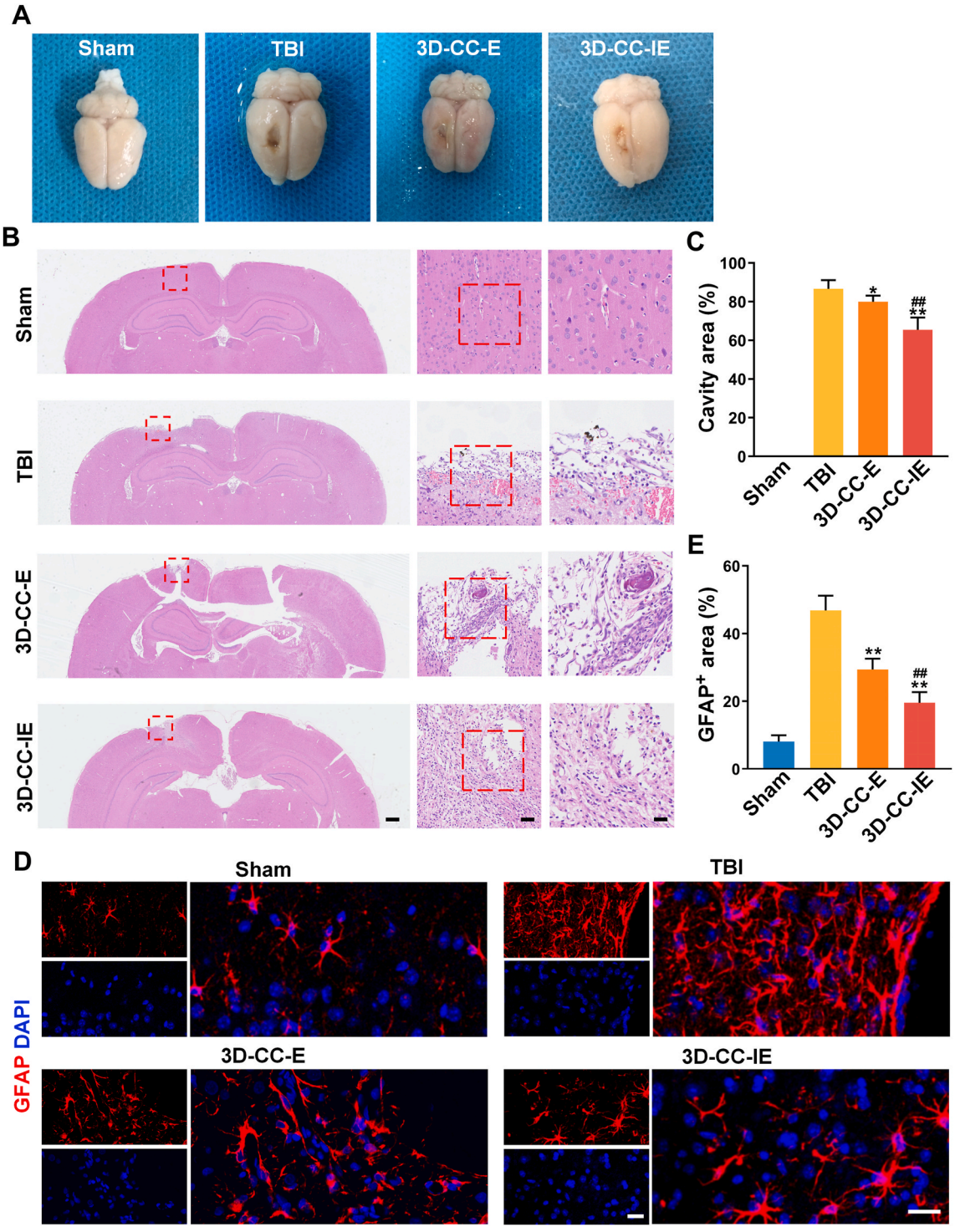

Fig. 6. The tissue remodeling in the lesion site after TBI in rats.
(A) Representative general views at 2 month after implantation among four groups. (B) Representative images of HE staining among four groups. (C) Statistical calculation of the cavity area per field. (D) The expression of GFAP around the lesion site among four groups. (E) Statistical calculation of $GFAP^+$ area per field. All data were expressed as mean ± SD; $^*P < 0.05$, $^{**}P < 0.01$ *vs.* TBI; $^{\#\#}P < 0.01$ *vs.* 3D-CC-E. Scale bars: 2 mm in (B left), 100 μm in (B, middle), 50 μm in (B, right and D).

volume in the 3D-CC-IE group compared to the TBI and 3D-CC-E groups (Fig. 6A). HE staining revealed fewer newly formed cells at the injury site in the TBI group, with neuronal nuclei shrinkage and cell deformation around the lesion (Fig. 6B). In the 3D-CC-E and 3D-CC-IE groups, newly formed cells were found around the lesion site. Compared to the TBI group (88.84 ± 4.663) and the 3D-CC-E group (79.73 ± 3.936), 3D-CC-IE implantation significantly reduced the cavity area (Fig. 6C). These results suggested that 3D-CC-IE implantation promoted regeneration in the lesion area following TBI. Similarly, a significant decrease in $GFAP^+$ cells indicated a marked reduction in glial scarring (Fig. 6D and E).

3.8. Implantation of 3D-CC-IE facilitated nerve fiber and myelin sheath regeneration

LFB resulted reveal myelin sheath loss following TBI (10.85 ± 1.0934). In contrast, the 3D-CC-E (18.43 ± 3.4799) and 3D-CC-IE (23.69

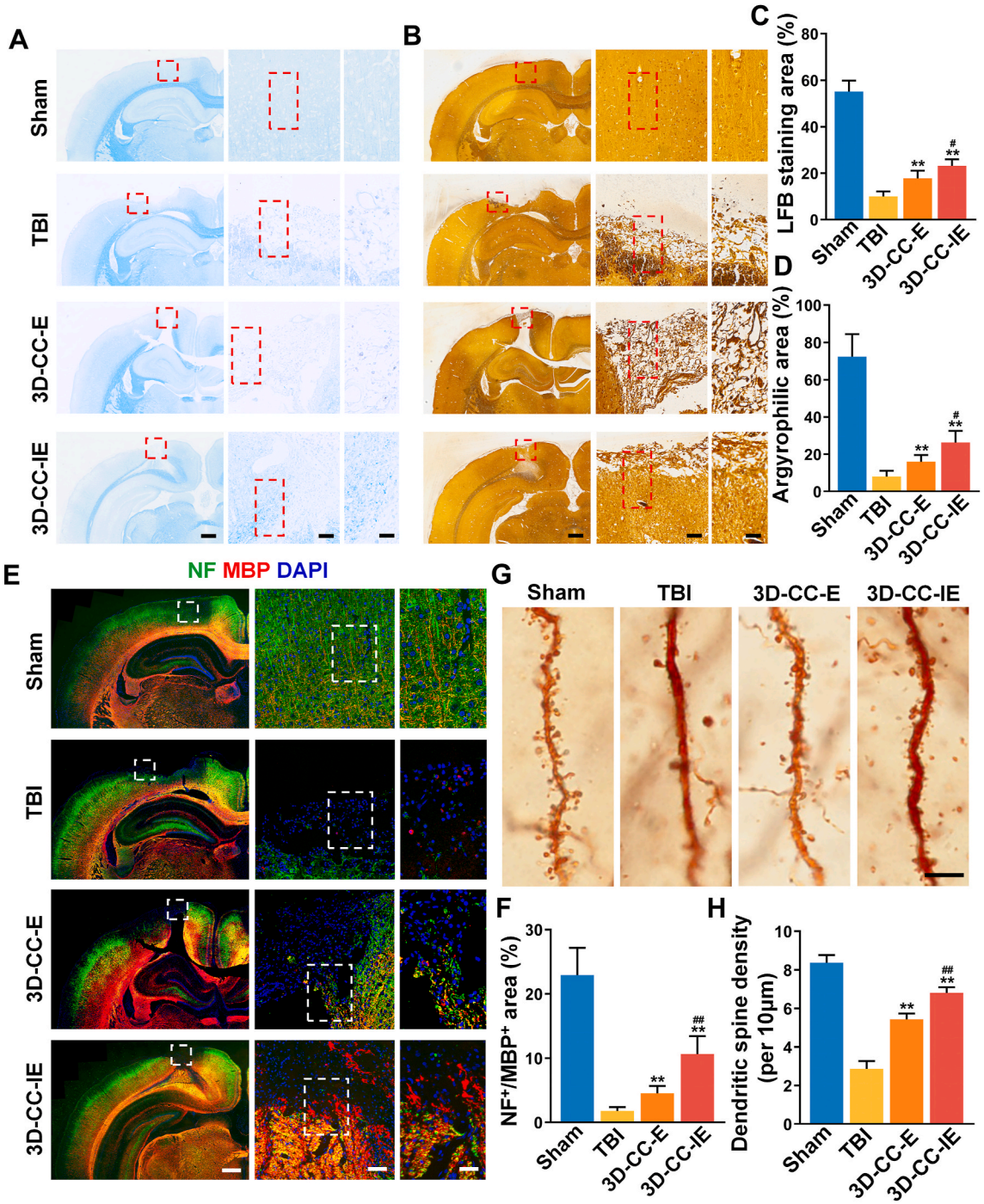

Fig. 7. The recovery of nerve fibers, myelin sheaths and dendritic spine at the lesion site of TBI. (A) Representative images of LFB staining at 2 month after implantation among four groups. (B) Representative images of Bielschowsky's silver staining at 2 month after implantation among four groups. (C and D) Statistical calculation of LFB staining area per field (C) and Argyrophilic area per field (D). (E) The expression of NF and MBP around the lesion site among four groups. (F) Statistical calculation of NF^+/MBP^+ area per field. (G) Representative images of Golgi staining at 2 month after implantation among four groups. (H) Statistical calculation of Dendritic spine density per 10 μm. All data were expressed as mean ± SD; $^{**}P < 0.01$ *vs.* TBI; $^{\#}P < 0.05$, $^{\#\#}P < 0.01$ *vs.* 3D-CC-E. Scale bars: 1 mm in (A, B and E left), 100 μm in (A, B and E middle), 50 μm in (A, B, and E right), 20 μm in (G).

± 2.8707) groups exhibited notable myelin sheath recovery, with particular emphasis on the significantly augmented myelin sheath density within the 3D-CC-IE group as compared to the 3D-CC-E group (Fig. 7A and C). Bielschowsky's silver staining of the 3D-CC-IE group (24.82 ± 6.477) demonstrated a conspicuous increase in nerve fibers and nascent neurons within the lesion site, unlike the TBI group (9.32 ± 2.024) and 3D-CC-E group (16.21 ± 3.023) (Fig. 7B and D). Dual immunofluorescent labeling of NF and MBP was conducted to assess nerve fibers and myelin sheaths in the lesion site. The 3D-CC-IE group displayed a higher abundance of NF^+ and MBP^+ cells in contrast to the TBI and 3D-CC-E groups (Fig. 7E and F). Golgi staining revealed dendritic spine morphological damage and a reduction in quantity after TBI. Recovery was observed following treatment with 3D-CC-E and 3D-CC-IE, with a significantly increased dendritic spine density in the 3D-CC-IE group compared to the 3D-CC-E group (Fig. 7G and H). These findings suggested that 3D-CC-IE implantation significantly augmented the restoration of nerve fibers and myelin sheaths within the TBI lesion site.

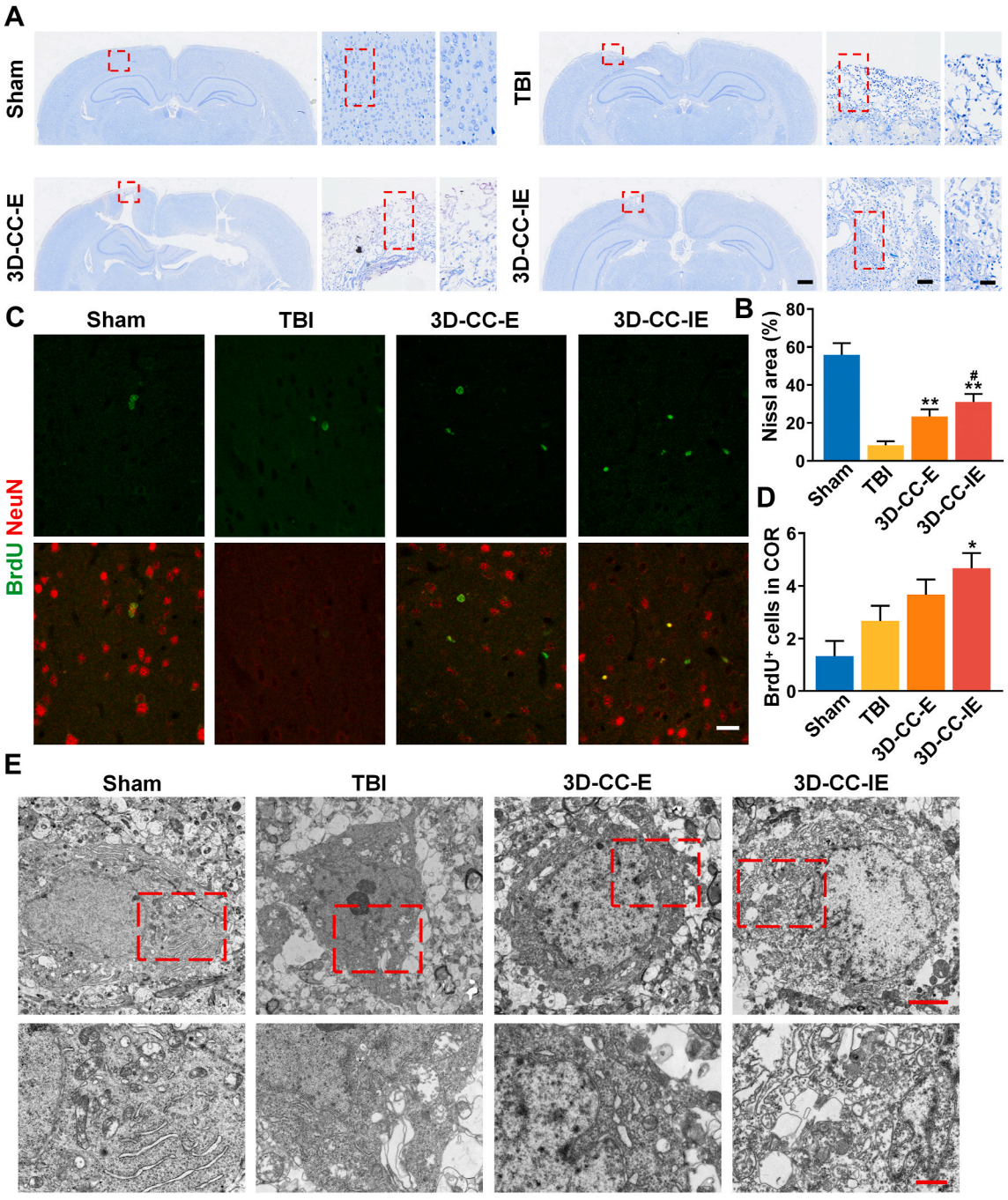

Fig. 8. 3D-CC-IE promoted endogenous neuroregeneration.
(A) Representative images of Nissl staining at 2 month after implantation among four groups. (B) Statistical calculation of $Nissl^+$ area per field. (C) Representative images of BrdU/NeuN in cortex among four groups. (D) Statistical calculation of $BrdU^+$ cells in cortex. (E) Representative TEM images of neurons at 2 month after implantation among four groups. All data were expressed as mean ± SD; $^{**}P < 0.01$ *vs.* TBI; $^{\#}P < 0.05$ *vs.* 3D-CC-E. Scale bars: 2 mm in (A left), 100 μm in (A middle), 50 μm in (A right and C), 25 μm in (C), 5 μm in (E).

3.9. 3D-CC-IE implantation significantly enhanced neuronal regeneration after TBI

To explore the potential mechanisms of 3D-CC-IE in treating TBI, brain tissue sections were histologically stained 2 months after TBI. Nissl staining revealed greater density and more widespread Nissl bodies in the 3D-CC-IE group (32.31 ± 2.427) compared to the TBI (7.09 ± 1.533) and 3D-CC-E (21.81 ± 3.569) groups (Fig. 8A and B). Further BrdU and

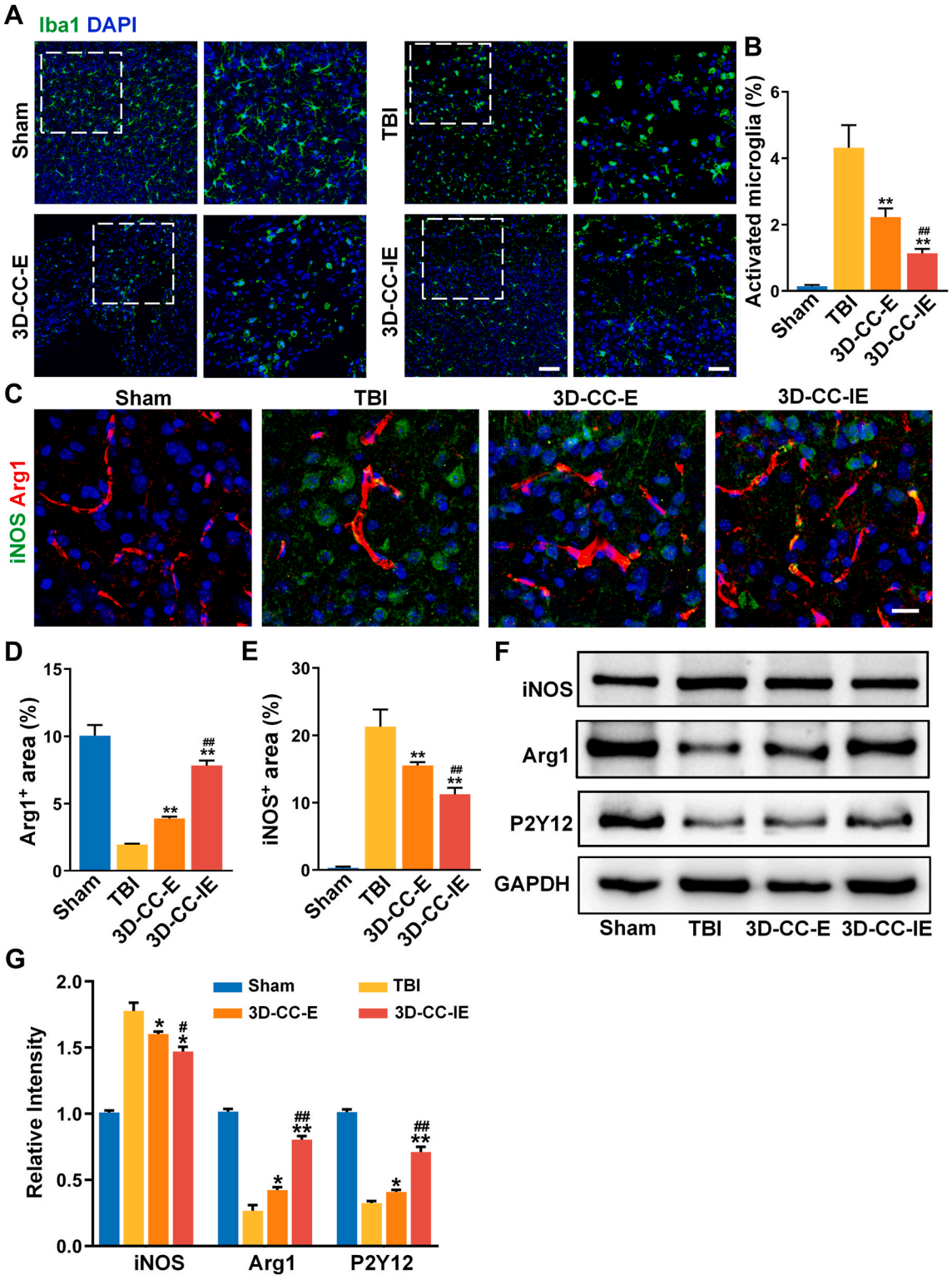

Fig. 9. The characterization of neuroinflammation in the lesion site after TBI in rats.
(A) Iba1 expression around the lesion site after TBI among four groups. (B) Statistical calculation of Activated microglia per field. (C) Arg1 and iNOS expression around the lesion site after TBI among four groups. (D and E) Statistical calculation of $Arg1^+$ (D) and $iNOS^+$ area per field (E). (F) Relative protein level (iNOS, Arg1 and P2Y12) among four groups. (G) Statistical calculation of relative protein intensity. All data were expressed as mean ± SD; $^*P < 0.05$, $^{**}P < 0.01$ *vs.* TBI; $^{\#}P < 0.05$, $^{\#\#}P < 0.01$ *vs.* 3D-CC-E. Scale bars: 100 μm in (A left), 50 μm in (A right) and 25 μm in (C).

NeuN labeling confirmed that the cortex initiated endogenous regeneration processes after TBI. The 3D-CC-IE group exhibited more BrdU$^+$ cells compared to the 3D-CC-E group, suggesting that IFN-Exo significantly promoted endogenous neuroregeneration (Fig. 8C and D). MAP2 immunofluorescence labeling was used to examine neuronal differentiation in the injured area after TBI. More MAP2$^+$ cells were found in the 3D-CC-IE group (15.71 ± 4.9962) than in the TBI (2.23 ± 0.5124) and 3D-CC-E (6.86 ± 2.1562) groups (Figs. S6A and B). TEM results also indicated the restoration of the ultrastructure within neurons of the 3D-CC-IE group (Fig. 8E). Von Willebrand factor (vWF) immunofluorescence staining was used to assess vascular regeneration in the lesion area after TBI. The 3D-CC-E (3.76 ± 0.8371) and 3D-CC-IE (8.92 ± 1.3274) groups exhibited more vWF-positive cells compared to the TBI group (2.88 ± 0.4052) (Figs. S6C and D). Furthermore, the degree of vascular regeneration was relatively higher in the 3D-CC-IE group than the 3D-CC-E group (Fig. S6D). Increased vascular formation over a larger area suggested that regenerating neurons in the injury zone can better survive. These findings collectively revealed that implantation of 3D-CC-IE after TBI promoted neuronal restoration.

3.10. 3D-CC-IE implantation reduced neuroinflammation

To assess inflammation in the lesion area after 3D-CC-IE implantation, iba1 immunofluorescence staining was employed. There was a significant increase in the expression of iba1$^+$ cells, which was markedly reduced in the lesion area by the 3D-CC-IE (0.51 ± 0.2142) group as compared to the TBI (4.25 ± 0.8804) and 3D-CC-E (1.42 ± 0.4055) groups (Fig. 9A and B). There was an increase in iNOS expression and a decrease in Arg1 within the lesion site after TBI, indicating the occurrence of neuroinflammation (Fig. 9C). However, the decreased expression of iNOS and the restored Arg1 in the 3D-CC-E and 3D-CC-IE groups confirmed the inhibition of neuroinflammation progression (Fig. 9D and E). Similarly, the results of Western blotting also demonstrated that after treatment with 3D-CC-E and 3D-CC-IE, the expression of iNOS decreased, while the expression of Arg1 and P2Y12 increased. This showed a transition of microglia from M1 to M2 phenotype (Fig. 9F and G). These results suggested that interferon-γ preconditioned exosomes might act on neural repair by suppressing neuroinflammation during TBI. To further validate the molecular mechanisms underlying the alleviation of neuroinflammation by IFN-Exo, we conducted additional western blotting experiments. The results of the western blotting indicated that the p38MAPK/mTOR signaling pathway was highly activated in the injury area after TBI, with significant increase in p-p38, p-ERK, TSC1, p-mTOR, and p-p70S6K (Fig. S7A). However, these levels decreased after 3D-CC-E treatment. Importantly, compared to 3D-CC-E group, 3D-CC-IE group exhibited a more pronounced effect in modulating the p38MAPK/mTOR signaling pathway (Figs. S7B–F).

4. Discussion

TBI caused mortality and disability globally. During the acute phase, neurons and axons underwent continuous death, with varying degrees of damage to vascular endothelium. This, in turn, allowed blood components, including peripheral immune cells, to infiltrate brain parenchyma, fostering a pro-inflammatory environment. Astrocytes swelled, leading to tissue edema, elevated intracranial pressure, reduced cerebral blood flow, ischemia, and exacerbation of a vicious cycle. This significantly prolonged the recovery time for TBI. Given the complexity of the pathophysiology involving interrelated immune, inflammatory, and neurovascular cascades following TBI, single-target treatments showed limited efficacy in clinical trials [50–52]. To address the intricate pathophysiological processes effectively, a combined therapy based on stem cell-derived exosomes and tissue engineering scaffolds was considered a potential strategy for TBI treatment. In this study, Exo and IFN-Exo, combined with a collagen/chitosan mixture, were used to fabricate 3D-CC-E and 3D-CC-IE scaffolds using low-temperature 3D printing technology. These printed scaffolds were directly transplanted into the injury site of TBI rats to investigate their therapeutic effects. Ultimately, improved neurological function, along with histological confirmation, substantiated the significant enhancement of neurofunctional recovery with the 3D-CC-IE therapy after TBI.

Exosomes derived from NSCs were considered a potential strategy for treating TBI [53,54]. Exosomes secreted by NSCs were rich in miRNAs and proteins involved in anti-apoptosis, anti-inflammatory effects, blood-brain barrier repair, promotion of neuronal regeneration, and synaptic plasticity. They played a crucial role in the extensive interaction between neurons and glial cells following TBI. Notably, exosomes subjected to various preconditioning conditions demonstrated robust therapeutic potential [23–25]. Previous studies had confirmed that IFN-γ-preconditioned exosomes effectively enhanced the recovery of neurological function after ischemic stroke in rats [29]. Therefore, we hypothesized that exosomes secreted by NSCs after IFN-γ preconditioning might have had potent therapeutic effects in TBI. In this study, we extracted and characterized exosomes using ultracentrifugation. We focused on the role of IFN-Exo and compared their functions with Exo. The results of miRNA sequencing showed that GO enrichment and KEGG enrichment of target genes in the IFN-Exo group mainly included both neural differentiation and inflammatory regulation. A large number of processes related to neural differentiation such as axon guidance, glutamatergic synapses, neuronal projections, and cAMP signaling pathway. These results suggested that IFN-Exo may promote the differentiation of NSCs to neurons, which may play a key auxiliary role in endogenous neurogenesis after TBI. The elevated expression of DCX and NeuN in the IFN-Exo group indicated that IFN-Exo promoted the differentiation and maturation of NSCs. Consistent with our sequencing results, related studies have demonstrated that miR-124, miR-7, and miR-21 promoted neural stem cell differentiation and maturation [55–57]. On the other hand, the IFN-Exo group exhibited processes related to inflammation regulation such as inflammatory response, PI3K-Akt signaling pathway, NF-κB signaling pathway and TGF-β signaling pathway. Consistency experiments with the sequencing results confirmed that IFN-Exo was able to inhibit the development of neuroinflammation as well as regulate the transition of M1-type microglia to M2-type. *In vitro* results confirmed that IFN-Exo attenuates neuroinflammation by modulating the MAPK/mTOR pathway. Published studies have confirmed that decreased miR-132 expression as well as upregulated miR-155 expression in neuroinflammatory states [58,59]. In addition, our results also revealed that IFN-Exo could increase the tolerance of primary neurons to OGD/R. Recent studies have shown that NSC-derived extracellular vesicles (NSC-EVs) can significantly improve the activation of microglia and reduce neuronal apoptosis after spinal cord injury in rats [60]. Additionally, one research has suggested that NSC-EVs can effectively promote the remodeling of brain tissue in pigs after ischemic stroke, including reducing brain lesion volume and edema [61]. In summary, IFN-Exo positively affected neuronal survival, axonal growth and vascular regeneration, and alleviated neuroinflammation, demonstrating that IFN-Exo had the potential to be involved in multiple pathophysiological processes in TBI, providing potential benefits for neurological recovery. Given the protracted course of TBI and the rapid clearance of exosomes, simple exosome therapy may not yield the most effective treatment outcomes [36,62]. Therefore, it is necessary to deliver exosomes via biomaterial scaffolds to maximize their retention and sustained release.

Numerous studies had substantiated the favorable mechanical properties and biocompatibility of composite scaffolds prepared from collagen and chitosan [63,64]. Additionally, being natural biomaterials, both collagen and chitosan could effectively mimic the ECM under physiological conditions, providing a necessary microenvironment for tissue repair [44]. Collagen, as a natural ECM protein, played a crucial role in cell adhesion and migration due to its excellent biocompatibility and low immunogenicity [65,66]. However, limitations such as rapid degradation and deformation hindered the suitability of a singular

collagen scaffold for tissue engineering [67]. Chitosan, acknowledged as a glycosaminoglycan, had demonstrated commendable properties such as hemostasis, antimicrobial activity, strong mechanical performance, and good cell compatibility, making it widely applied in biomedical fields like wound healing, drug delivery vehicles, and peripheral nerve regeneration [68,69]. Nevertheless, due to its low hydrophilicity, chitosan's biodegradability was not fully optimal [70]. Therefore, adjusting the biodegradation rate of chitosan to better match the pace of new tissue formation held crucial significance for neural tissue regeneration. Previous research had confirmed that chitosan and collagen were molecularly soluble and exhibited interaction between components [71]. Multiple studies suggested the pivotal role of collagen and chitosan in the reconstruction of neural networks after central nervous system injuries [24,25,72]. Thus, in this study, we utilized low-temperature 3D printing technology to fabricate collagen/chitosan scaffolds, maximizing the preservation of exosome activity. The 3D-printed scaffolds prepared in this study exhibited a higher elastic modulus, facilitating the attachment and migration of endogenous NSCs within the scaffold. The porosity of 3D-CC-IE was higher than that of CC scaffolds, possibly contributing to the larger release of exosomes in 3D-CC-IE compared to CC-IE. Additionally, SEM indicated multiple internal voids within the scaffold, with exosomes adhering to its inner surface. Furthermore, three-dimensional reconstructed fluorescent images demonstrated the distribution of exosomes within the scaffold. Adequate water absorption rates allowed the scaffold to effectively load exosomes and prevent their loss, supporting cell growth. In this study, we observed a significantly higher release of exosomes from the 3D-CC-IE scaffold compared to the CC-IE scaffold, revealing that 3D printing technology enhanced the fixation and release capabilities of collagen/chitosan, and the released exosomes could be engulfed by NSCs. In conclusion, these results suggested that the 3D-printed CC scaffold enabled the uniform distribution of exosomes and maintained a higher release rate. Subsequently, we loaded the exosomes onto a chitosan-collagen (CC) scaffold and co-cultured them with NSCs. The results showed that IFN-Exo exhibited higher cellular viability and adhesion rates compared to ordinary exosomes when incorporated into the CC scaffold. These findings confirmed the promising potential of 3D-CC-IE in the treatment of TBI.

The results unequivocally demonstrated that exosomes released from the 3D-CC-IE scaffold played a crucial role in the lesion site after TBI. Firstly, we implanted 3D-CC-IE into the cortical lesion area of rats after TBI, and significant improvements in mNSS scores and various indicators in the water maze suggested that 3D-CC-IE promoted cognitive function recovery after TBI. Meanwhile, *in vivo* experiments showed that 3D-CC-IE possessed good biocompatibility and was non-toxic to the organism, making it an ideal choice for treating TBI. Subsequent histological staining confirmed the potential contribution of 3D-CC-IE to long-term neural function recovery after TBI. Improvements in histological morphology (HE staining, Bielschowsky's silver staining, Nissl staining, LFB staining, Golgi staining and immunofluorescence staining) and ultrastructure within neurons after 2 months suggested that 3D-CC-IE effectively reduced neuronal damage and promoted tissue reconstruction in the lesion site. Consistent with miRNA sequencing, the elevation of MAP2 indicated that 3D-CC-IE significantly enhanced the differentiation of NSCs, as well as endogenous neurogenesis in cortical regions, suggesting enhanced endogenous neurogenesis after TBI. Meanwhile, another crucial factor influencing brain repair after TBI was vascular regeneration. In this study, 3D-CC-IE promoted the expression of von willebrand factor (vWF) in the lesion area, demonstrating that IFN-Exo significantly facilitated vascular remodeling, which favored the survival and development of regenerating neurons. Neuroinflammation is a crucial process in the pathological physiology of TBI, involving activation of glial cells, infiltration of inflammatory cells, and secretion of pro-inflammatory factors [73]. The differential expression of iba1, Arg1 and iNOS in this research confirmed that 3D-CC-IE significantly alleviated microglia activation at the lesion site and promoted its transition from M1-type to M2-type. Whereas *in vivo* and *in vitro* experiments jointly confirmed that IFN-Exo alleviated secondary neuroinflammation by modulating the MAPK/mTOR signaling pathway.

Our research revealed that IFN-Exo actively participated in various pathophysiological processes after TBI. Consistent results from miRNA sequencing and *in vivo* experiments confirmed that IFN-Exo promoted neural differentiation and reduced neuroinflammation, which provided a specific microenvironment to accelerate the neuroregenerative effects of 3D-CC-IE. Thanks to the rich abundance and strong targeting of functional proteins and miRNA in IFN-Exo, 3D-CC-IE significantly promoted neural network reconstruction and neurofunctional recovery. As mentioned earlier, the therapeutic effects of exosomes on TBI result from the combined action of multiple factors rather than a single element. In this study, IFN-Exo was loaded onto a CC scaffold using low-temperature 3D printing technology, which extended the duration of exosome action, aligning it with the process of TBI recovery and thus exerting powerful therapeutic effects. Future research should focus on exploring cellular developmental trajectories and interactions during tissue repair, providing feasible timelines for scaffold design and exosomes release. For instance, tracking the distribution of exosomes in the lesion area and the developmental status of regenerated neurons. Additionally, recent studies have confirmed that nanoparticle-based drug delivery or nanoscaffolds exhibited promising therapeutic effects for TBI [74–76]. Given that nanoparticles can achieve effective encapsulation and targeted delivery of exosomes, they may become a focus of future research directions.

5. Conclusions

In this study, we proposed a potential therapeutic strategy for TBI based on interferon-γ-preconditioned NSC-derived exosomes (IFN-Exo) and 3D-printed collagen/chitosan scaffolds (3D-CC-IE). IFN-Exo showed potent ability to promote NSC differentiation as well as reduce neuroinflammation. The 3D-CC-IE scaffold exhibited excellent biological and mechanical properties, providing a suitable microenvironment for NSCs differentiation and exosomes release. Additionally, the 3D-CC-IE scaffold participated in multiple pathological processes after rat TBI, significantly improving neurodeficiency. In summary, the 3D-CC-IE therapy had a positive impact on enhancing neuroregeneration after TBI, presenting significant clinical application potential.

Funding

This work was supported by the National Key Research and Development Program of China (2021YFF1200800, 2018YFA0108700), the National Natural Science Foundation of China (82171861, 82170256, 82101448), Guangdong Provincial Special Support Program for Prominent Talents (2021JC06Y656), Science and Technology Planning Project of Guangdong Province (2020B1111170011, 2022B1212010010), Guangzhou Science and Technology Plan Project (202201000006), the Natural Science Foundation of Sichuan Province (24NSFSC3547).

Ethics approval and consent to participate

All animal procedures involving animals were conducted in accordance with the approved protocol for the care and use of laboratory animals by the Animal Care Committee of Tianjin University (Ethical approval number: 23658/42, Animal license number: SYXK (Jin) 2021-0003). All the authors compliance with all relevant ethical regulations.

CRediT authorship contribution statement

Chong Chen: Data curation, Conceptualization. **Zhe-Han Chang:** Writing – original draft, Visualization, Methodology. **Bin Yao:** Investigation, Data curation. **Xiao-Yin Liu:** Validation, Formal analysis. **Xiao-Wang Zhang:** Formal analysis. **Jun Liang:** Resources. **Jing-Jing Wang:** Formal analysis, Data curation. **Shuang-Qing Bao:** Software, Resources.

Meng-Meng Chen: Software, Resources. **Ping Zhu:** Project administration, Investigation. **Xiao-Hong Li:** Supervision, Project administration, Funding acquisition.

Declaration of competing interest

The authors report no competing interests.

Abbreviations

TBI	Traumatic brain injury
NSCs	neural stem cells
IFN	IFN-γ
IE	IFN-γ preconditioned exosomes
BBB	blood-brain barrier
CNS	central nervous system
ECM	extracellular matrix
CC	collagen-chitosan
LPS	Lipopolysaccharide
OGD/R	oxygen-glucose deprivation/reperfusion
ANI	Anisomycin
3D-CC-E	3D-printed collagen/chitosan scaffolds integrated with NSC exosomes
3D-CC-IE	3D-printed collagen/chitosan scaffolds integrated with IFN preconditioned NSC exosomes
MTT	methylthiazolyldiphenyl-tetrazoliumbromide
mNSS	Modified neurological severity score
TEM	Transmission electron microscopy
SEM	Scanning Electron microscopy
MWM	Morris water maze
LFB	Luxol Fast Blue staining
GO	Gene Ontology
KEGG	Kyoto Encyclopedia of Genes and Genomes
BDNF	Brain-derived neurotrophic factor
GDNF	Glia cell line-derived neurotrophic factor
ALT	alanine aminotransferase
CR	creatinine
AST	aspartate aminotransferase
BUN	blood urea nitrogen
NSC-EVs	NSC-derived extracellular vesicles

Appendix A. Supplementary data

Supplementary data to this article can be found online at https://doi.org/10.1016/j.bioactmat.2024.05.026.

References

[1] N. The Lancet, The future research path of traumatic brain injury, Lancet Neurol. 21 (4) (2022) 295.

[2] J.Y. Jiang, G.Y. Gao, J.F. Feng, Q. Mao, L.G. Chen, X.F. Yang, J.F. Liu, Y.H. Wang, B.H. Qiu, X.J. Huang, Traumatic brain injury in China, Lancet Neurol. 18 (3) (2019) 286–295.

[3] F. Panza, R. Sardone, V. Dibello, A. Daniele, V. Solfrizzi, M. Lozupone, Frailty and outcome after traumatic brain injury, Lancet Neurol. 21 (2) (2022) 107–108.

[4] A.I.R. Maas, D.K. Menon, G.T. Manley, M. Abrams, C. Akerlund, N. Andelic, M. Aries, T. Bashford, M.J. Bell, Y.G. Bodien, B.L. Brett, A. Buki, R.M. Chesnut, G. Citerio, D. Clark, B. Clasby, D.J. Cooper, E. Czeiter, M. Czosnyka, K. Dams-O'Connor, V. De Keyser, R. Diaz-Arrastia, A. Ercole, T.A. van Essen, E. Falvey, A. R. Ferguson, A. Figaji, M. Fitzgerald, B. Foreman, D. Gantner, G. Gao, J. Giacino, B. Gravesteijn, F. Guiza, D. Gupta, M. Gurnell, J.A. Haagsma, F.M. Hammond, G. Hawryluk, P. Hutchinson, M. van der Jagt, S. Jain, S. Jain, J.Y. Jiang, H. Kent, A. Kolias, E.J.O. Kompanje, F. Lecky, H.F. Lingsma, M. Maegele, M. Majdan, A. Markowitz, M. McCrea, G. Meyfroidt, A. Mikolic, S. Mondello, P. Mukherjee, D. Nelson, L.D. Nelson, V. Newcombe, D. Okonkwo, M. Oresic, W. Peul, D. Pisica, S. Polinder, J. Ponsford, L. Puybasset, R. Raj, C. Robba, C. Roe, J. Rosand, P. Schueler, D.J. Sharp, P. Smielewski, M.B. Stein, N. von Steinbuchel, W. Stewart, E.W. Steyerberg, N. Stocchetti, N. Temkin, O. Tenovuo, A. Theadom, I. Thomas, A. T. Espin, A.F. Turgeon, A. Unterberg, D. Van Praag, E. van Veen, J. Verheyden, T. V. Vyvere, K.K.W. Wang, E.J.A. Wiegers, W.H. Williams, L. Wilson, S. R. Wisniewski, A. Younsi, J.K. Yue, E.L. Yuh, F.A. Zeiler, M. Zeldovich, R. Zemek, T.P. In, Investigators, Traumatic brain injury: progress and challenges in prevention, clinical care, and research, Lancet Neurol. 21 (11) (2022) 1004–1060.

[5] J. Zhang, X. Liu, K. Ma, M. Chen, H. Xu, X. Niu, H. Gu, R. Wang, X. Chen, H. Sun, Collagen/heparin scaffold combined with vascular endothelial growth factor promotes the repair of neurological function in rats with traumatic brain injury, Biomater. Sci. 9 (3) (2021) 745–764.

[6] X.Y. Liu, Z.H. Chang, C. Chen, J. Liang, J.X. Shi, X. Fan, Q. Shao, W.W. Meng, J. J. Wang, X.H. Li, 3D printing of injury-preconditioned secretome/collagen/heparan sulfate scaffolds for neurological recovery after traumatic brain injury in rats, Stem Cell Res. Ther. 13 (1) (2022) 525.

[7] L. Zhong, J. Wang, P. Wang, X. Liu, P. Liu, X. Cheng, L. Cao, H. Wu, J. Chen, L. Zhou, Neural stem cell-derived exosomes and regeneration: cell-free therapeutic strategies for traumatic brain injury, Stem Cell Res. Ther. 14 (1) (2023) 198.

[8] F. Qian, Y. Han, Z. Han, D. Zhang, L. Zhang, G. Zhao, S. Li, G. Jin, R. Yu, H. Liu, In Situ implantable, post-trauma microenvironment-responsive, ROS Depletion Hydrogels for the treatment of Traumatic brain injury, Biomaterials 270 (2021) 120675.

[9] X. Li, E. Sundstrom, Stem cell therapies for central nervous system trauma: the 4 Ws-what, when, where, and why, Stem Cells Transl Med 11 (1) (2022) 14–25.

[10] Y. Xiong, A. Mahmood, M. Chopp, Emerging potential of exosomes for treatment of traumatic brain injury, Neural Regen Res 12 (1) (2017) 19–22.

[11] W. Liu, X. Bai, A. Zhang, J. Huang, S. Xu, J. Zhang, Role of exosomes in central nervous system diseases, Front. Mol. Neurosci. 12 (2019) 240.

[12] C. Gu, Y. Li, J. Liu, S. Liu, J. Long, Q. Zhang, W. Duan, T. Feng, J. Huang, Y. Qiu, W. Ahmed, H. Cai, Y. Hu, Y. Wu, L. Chen, Neural stem cell-derived exosomes-loaded adhesive hydrogel controlled-release promotes cerebral angiogenesis and neurological function in ischemic stroke, Exp. Neurol. 370 (2023) 114547.

[13] X. Zhao, J. Zhu, S. Chen, R. Liu, T. Long, Neural stem cell-derived exosomes improve neurological function in rats with cerebral ischemia-reperfusion injury by regulating microglia-mediated inflammatory response, J. Inflamm. Res. 16 (2023) 3079–3092.

[14] Z.H. Zhu, F. Jia, W. Ahmed, G.L. Zhang, H. Wang, C.Q. Lin, W.H. Chen, L.K. Chen, Neural stem cell-derived exosome as a nano-sized carrier for BDNF delivery to a rat model of ischemic stroke, Neural Regen Res 18 (2) (2023) 404–409.

[15] B. Gyorgy, M.E. Hung, X.O. Breakefield, J.N. Leonard, Therapeutic applications of extracellular vesicles: clinical promise and open questions, Annu. Rev. Pharmacol. Toxicol. 55 (2015) 439–464.

[16] Z.G. Zhang, M. Chopp, Exosomes in stroke pathogenesis and therapy, J. Clin. Invest. 126 (4) (2016) 1190–1197.

[17] Y.Y. Xiong, Z.T. Gong, R.J. Tang, Y.J. Yang, The pivotal roles of exosomes derived from endogenous immune cells and exogenous stem cells in myocardial repair after acute myocardial infarction, Theranostics 11 (3) (2021) 1046–1058.

[18] K. Moeinabadi-Bidgoli, M. Rezaee, H. Rismanchi, M.M. Mohammadi, A. Babajani, Mesenchymal stem cell-derived antimicrobial peptides as potential anti-neoplastic agents: new insight into anticancer mechanisms of stem cells and exosomes, Front. Cell Dev. Biol. 10 (2022) 900418.

[19] G.E. Manuel, T. Johnson, D. Liu, Therapeutic angiogenesis of exosomes for ischemic stroke, Int J Physiol Pathophysiol Pharmacol 9 (6) (2017) 188–191.

[20] L. Li, J. Mu, Y. Zhang, C. Zhang, T. Ma, L. Chen, T. Huang, J. Wu, J. Cao, S. Feng, Y. Cai, M. Han, J. Gao, Stimulation by exosomes from hypoxia preconditioned human umbilical vein endothelial cells facilitates mesenchymal stem cells angiogenic function for spinal cord repair, ACS Nano 16 (7) (2022) 10811–10823.

[21] Y. Shi, Y. Wang, Q. Li, K. Liu, J. Hou, C. Shao, Y. Wang, Immunoregulatory mechanisms of mesenchymal stem and stromal cells in inflammatory diseases, Nat. Rev. Nephrol. 14 (8) (2018) 493–507.

[22] X. Liu, C. Wu, Y. Zhang, S. Chen, J. Ding, Z. Chen, K. Wu, X. Wu, T. Zhou, M. Zeng, D. Wei, J. Sun, H. Fan, L. Zhou, Hyaluronan-based hydrogel integrating exosomes for traumatic brain injury repair by promoting angiogenesis and neurogenesis, Carbohydr. Polym. 306 (2023) 120578.

[23] Y.C. Ye, Z.H. Chang, P. Wang, Y.W. Wang, J. Liang, C. Chen, J.J. Wang, H.T. Sun, Y. Wang, X.H. Li, Infarct-preconditioning exosomes of umbilical cord mesenchymal stem cells promoted vascular remodeling and neurological recovery after stroke in rats, Stem Cell Res. Ther. 13 (1) (2022) 378.

[24] X. Liu, J. Zhang, X. Cheng, P. Liu, Q. Feng, S. Wang, Y. Li, H. Gu, L. Zhong, M. Chen, L. Zhou, Integrated printed BDNF-stimulated HUCMSCs-derived exosomes/collagen/chitosan biological scaffolds with 3D printing technology promoted the remodelling of neural networks after traumatic brain injury, Regen Biomater 10 (2023) rbac085.

[25] X.Y. Liu, Y.H. Feng, Q.B. Feng, J.Y. Zhang, L. Zhong, P. Liu, S. Wang, Y.R. Huang, X.Y. Chen, L.X. Zhou, Low-temperature 3D-printed collagen/chitosan scaffolds loaded with exosomes derived from neural stem cells pretreated with insulin growth factor-1 enhance neural regeneration after traumatic brain injury, Neural Regen Res 18 (9) (2023) 1990–1998.

[26] Y. Li, C. Ren, H. Li, F. Jiang, L. Wang, C. Xia, X. Ji, Role of exosomes induced by remote ischemic preconditioning in neuroprotection against cerebral ischemia, Neuroreport 30 (12) (2019) 834–841.

[27] N. Hu, Z. Cai, X. Jiang, C. Wang, T. Tang, T. Xu, H. Chen, X. Li, X. Du, W. Cui, Hypoxia-pretreated ADSC-derived exosome-embedded hydrogels promote angiogenesis and accelerate diabetic wound healing, Acta Biomater. 157 (2023) 175–186.

[28] G. Zhang, X. Guo, L. Chen, B. Li, B. Gu, H. Wang, G. Wu, J. Kong, W. Chen, Y. Yu, Interferon-gamma promotes neuronal repair by transplanted neural stem cells in ischemic rats, Stem Cell. Dev. 27 (5) (2018) 355–366.

[29] G. Zhang, Z. Zhu, H. Wang, Y. Yu, W. Chen, A. Waqas, Y. Wang, L. Chen, Exosomes derived from human neural stem cells stimulated by interferon gamma improve therapeutic ability in ischemic stroke model, J. Adv. Res. 24 (2020) 435–445.

[30] G. Wong, Y. Goldshmit, M.A. Turnley, Interferon-g but not TNFa promotes neuronal differentiation and neurite outgrowth of murine adult neural stem cells, Exp. Neurol. 187 (1) (2004) 171–177.
[31] S.J. Kim, T.G. Son, K. Kim, H.R. Park, M.P. Mattson, J. Lee, Interferon-gamma promotes differentiation of neural progenitor cells via the JNK pathway, Neurochem. Res. 32 (8) (2007) 1399–1406.
[32] N.D. Leipzig, C. Xu, T. Zahir, M.S. Shoichet, Functional immobilization of interferon-gamma induces neuronal differentiation of neural stem cells, J. Biomed. Mater. Res. 93 (2) (2010) 625–633.
[33] G. Zhang, L. Chen, W. Chen, B. Li, Y. Yu, F. Lin, X. Guo, H. Wang, G. Wu, B. Gu, W. Miao, J. Kong, X. Jin, G. Yi, Y. You, X. Su, N. Gu, Neural stem cells alleviate inflammation via neutralization of IFN-gamma negative effect in ischemic stroke model, J. Biomed. Nanotechnol. 14 (6) (2018) 1178–1188.
[34] D. Carvajal Ibañez, M. Skabkin, J. Hooli, S. Cerrizuela, M. Göpferich, A. Jolly, K. Volk, M. Zumwinkel, M. Bertolini, G. Figlia, T. Höfer, G. Kramer, S. Anders, A. A. Teleman, A. Marciniak-Czochra, A. Martin-Villalba, Interferon regulates neural stem cell function at all ages by orchestrating mTOR and cell cycle, EMBO Mol. Med. 15 (4) (2023) e16434.
[35] C. Cossetti, N. Iraci, T.R. Mercer, T. Leonardi, E. Alpi, D. Drago, C. Alfaro-Cervello, H.K. Saini, M.P. Davis, J. Schaeffer, B. Vega, M. Stefanini, C. Zhao, W. Muller, J. M. Garcia-Verdugo, S. Mathivanan, A. Bachi, A.J. Enright, J.S. Mattick, S. Pluchino, Extracellular vesicles from neural stem cells transfer IFN-gamma via Ifngr1 to activate Stat1 signaling in target cells, Mol. Cell 56 (2) (2014) 193–204.
[36] D.W. Simon, M.J. McGeachy, H. Bayır, R.S.B. Clark, D.J. Loane, P.M. Kochanek, The far-reaching scope of neuroinflammation after traumatic brain injury, Nat. Rev. Neurol. 13 (3) (2017) 171–191.
[37] T. Chen, Y. Xia, L. Zhang, T. Xu, Y. Yi, J. Chen, Z. Liu, L. Yang, S. Chen, X. Zhou, X. Chen, H. Wu, J. Liu, Loading neural stem cells on hydrogel scaffold improves cell retention rate and promotes functional recovery in traumatic brain injury, Mater Today Bio 19 (2023) 100606.
[38] C.A. Martin, S. Radhakrishnan, J.L. Gomez Ribelles, O.A. Trentz, N. Eak, M. S. Reddy, M. Rela, N. Kalkura Subbaraya, Adipose tissue derived stromal cells in a gelatin-based 3D matrix with exclusive ascorbic acid signalling emerged as a novel neural tissue engineering construct: an innovative prototype for soft tissue, Regen Biomater 9 (2022) rbac031.
[39] G.D. Mahumane, P. Kumar, V. Pillay, Y.E. Choonara, Repositioning N-acetylcysteine (NAC): NAC-loaded electrospun drug delivery scaffolding for potential neural tissue engineering application, Pharmaceutics 12 (10) (2020).
[40] A. Lee, A.R. Hudson, D.J. Shiwarski, J.W. Tashman, T.J. Hinton, S. Yerneni, J. M. Bliley, P.G. Campbell, A.W. Feinberg, 3D bioprinting of collagen to rebuild components of the human heart, Science 365 (6452) (2019) 482–487.
[41] L. Wang, J.P. Stegemann, Thermogelling chitosan and collagen composite hydrogels initiated with beta-glycerophosphate for bone tissue engineering, Biomaterials 31 (14) (2010) 3976–3985.
[42] D. Zhang, X. Wu, J. Chen, K. Lin, The development of collagen based composite scaffolds for bone regeneration, Bioact. Mater. 3 (1) (2018) 129–138.
[43] E.O. Osidak, P.A. Karalkin, M.S. Osidak, V.A. Parfenov, D.E. Sivogrivov, F. Pereira, A.A. Gryadunova, E.V. Koudan, Y.D. Khesuani, C.V.A. capital Ka, S.I. Belousov, S. V. Krasheninnikov, T.E. Grigoriev, S.N. Chvalun, E.A. Bulanova, V.A. Mironov, S. P. Domogatsky, Viscoll collagen solution as a novel bioink for direct 3D bioprinting, J. Mater. Sci. Mater. Med. 30 (3) (2019) 31.
[44] Y. Sun, C. Yang, X. Zhu, J.J. Wang, X.Y. Liu, X.P. Yang, X.W. An, J. Liang, H. J. Dong, W. Jiang, C. Chen, Z.G. Wang, H.T. Sun, Y. Tu, S. Zhang, F. Chen, X.H. Li, 3D printing collagen/chitosan scaffold ameliorated axon regeneration and neurological recovery after spinal cord injury, J. Biomed. Mater. Res. 107 (9) (2019) 1898–1908.
[45] S. Azizian, A. Hadjizadeh, H. Niknejad, Chitosan-gelatin porous scaffold incorporated with Chitosan nanoparticles for growth factor delivery in tissue engineering, Carbohydr. Polym. 202 (2018) 315–322.
[46] P. Hao, H. Duan, F. Hao, L. Chen, M. Sun, K.S. Fan, Y.E. Sun, D. Williams, Z. Yang, X. Li, Neural repair by NT3-chitosan via enhancement of endogenous neurogenesis after adult focal aspiration brain injury, Biomaterials 140 (2017) 88–102.
[47] F. Yan, M. Li, H.Q. Zhang, G.L. Li, Y. Hua, Y. Shen, X.M. Ji, C.J. Wu, H. An, M. Ren, Collagen-chitosan scaffold impregnated with bone marrow mesenchymal stem cells for treatment of traumatic brain injury, Neural Regen Res 14 (10) (2019) 1780–1786.
[48] X.Y. Liu, C. Chen, H.H. Xu, Y.S. Zhang, L. Zhong, N. Hu, X.L. Jia, Y.W. Wang, K. H. Zhong, C. Liu, X. Zhu, D. Ming, X.H. Li, Integrated printed BDNF/collagen/chitosan scaffolds with low temperature extrusion 3D printer accelerated neural regeneration after spinal cord injury, Regen Biomater 8 (6) (2021) rbab047.
[49] X. Feng, P. Xu, T. Shen, Y. Zhang, J. Ye, C. Gao, Influence of pore architectures of silk fibroin/collagen composite scaffolds on the regeneration of osteochondral defects in vivo, J. Mater. Chem. B 8 (3) (2020) 391–405.
[50] M. Carbonara, F. Fossi, T. Zoerle, F. Ortolano, F. Moro, F. Pischiutta, E.R. Zanier, N. Stocchetti, Neuroprotection in traumatic brain injury: mesenchymal stromal cells can potentially overcome some limitations of previous clinical trials, Front. Neurol. 9 (2018) 885.
[51] S. Chakraborty, B. Skolnick, R.K. Narayan, Neuroprotection trials in traumatic brain injury, Curr. Neurol. Neurosci. Rep. 16 (4) (2016) 29.
[52] C.S. Cox Jr., J. Juranek, S. Bedi, Clinical trials in traumatic brain injury: cellular therapy and outcome measures, Transfusion 59 (S1) (2019) 858–868.
[53] A. Badner, E.K. Reinhardt, T.V. Nguyen, N. Midani, A.T. Marshall, C.A. Lepe, K. Echeverria, J.J. Lepe, V. Torrecampo, S.H. Bertan, S.H. Tran, A.J. Anderson, B. J. Cummings, Freshly thawed cryobanked human neural stem cells engraft within endogenous neurogenic niches and restore cognitive function after chronic traumatic brain injury, J. Neurotrauma 38 (19) (2021) 2731–2746.
[54] C. Hering, A.K. Shetty, Extracellular vesicles derived from neural stem cells, astrocytes, and microglia as therapeutics for easing TBI-induced brain dysfunction, Stem Cells Transl Med 12 (3) (2023) 140–153.
[55] J. Liu, J. Githinji, B. McLaughlin, K. Wilczek, J. Nolta, Role of miRNAs in neuronal differentiation from human embryonic stem cell-derived neural stem cells, Stem Cell Rev Rep 8 (4) (2012) 1129–1137.
[56] W.M. Zhang, Z.R. Zhang, X.T. Yang, Y.G. Zhang, Y.S. Gao, Overexpression of miR-21 promotes neural stem cell proliferation and neural differentiation via the Wnt/β-catenin signaling pathway in vitro, Mol. Med. Rep. 17 (1) (2018) 330–335.
[57] S. Jiao, Y. Liu, Y. Yao, J. Teng, miR-124 promotes proliferation and neural differentiation of neural stem cells through targeting DACT1 and activating Wnt/β-catenin pathways, Mol. Cell. Biochem. 449 (1–2) (2018) 305–314.
[58] H. Kong, F. Yin, F. He, A. Omran, L. Li, T. Wu, Y. Wang, J. Peng, The Effect of miR-132, miR-146a, and miR-155 on MRP8/TLR4-Induced Astrocyte-Related Inflammation, J. Mol. Neurosci. 57 (1) (2015) 28–37.
[59] A. Korotkov, N. Puhakka, S.D. Gupta, N. Vuokila, D.W.M. Broekaart, J.J. Anink, M. Heiskanen, J. Karttunen, J. van Scheppingen, I. Huitinga, J.D. Mills, E.A. van Vliet, A. Pitkänen, E. Aronica, Increased expression of miR142 and miR155 in glial and immune cells after traumatic brain injury may contribute to neuroinflammation via astrocyte activation, Brain Pathol. 30 (5) (2020) 897–912.
[60] Y. Rong, W. Liu, J. Wang, J. Fan, Y. Luo, L. Li, F. Kong, J. Chen, P. Tang, W. Cai, Neural stem cell-derived small extracellular vesicles attenuate apoptosis and neuroinflammation after traumatic spinal cord injury by activating autophagy, Cell Death Dis. 10 (5) (2019) 340.
[61] R.L. Webb, E.E. Kaiser, B.J. Jurgielewicz, S. Spellicy, S.L. Scoville, T.A. Thompson, R.L. Swetenburg, D.C. Hess, F.D. West, S.L. Stice, Human neural stem cell extracellular vesicles improve recovery in a porcine model of ischemic stroke, Stroke 49 (5) (2018) 1248–1256.
[62] Y.-J. Li, J.-Y. Wu, J. Liu, W. Xu, X. Qiu, S. Huang, X.-B. Hu, D.-X. Xiang, Artificial exosomes for translational nanomedicine, J. Nanobiotechnol. 19 (1) (2021) 242.
[63] K.I. Lukanina, T.E. Grigoriev, S.V. Krasheninnikov, V.G. Mamagulashvilli, R. A. Kamyshinsky, S.N. Chvalun, Multi-hierarchical tissue-engineering ECM-like scaffolds based on cellulose acetate with collagen and chitosan fillers, Carbohydr. Polym. 191 (2018) 119–126.
[64] G. Li, Q. Han, P. Lu, L. Zhang, Y. Zhang, S. Chen, P. Zhang, L. Zhang, W. Cui, H. Wang, H. Zhang, Construction of Dual-Biofunctionalized Chitosan/Collagen Scaffolds for Simultaneous Neovascularization and Nerve Regeneration, vol. 2020, Research (Wash D C), 2020 2603048.
[65] Y. Zou, Y. Yin, Z. Xiao, Y. Zhao, J. Han, B. Chen, B. Xu, Y. Cui, X. Ma, J. Dai, Transplantation of collagen sponge-based three-dimensional neural stem cells cultured in a RCCS facilitates locomotor functional recovery in spinal cord injury animals, Biomater. Sci. 10 (4) (2022) 915–924.
[66] C.M. Murphy, M.G. Haugh, F.J. O'Brien, The effect of mean pore size on cell attachment, proliferation and migration in collagen-glycosaminoglycan scaffolds for bone tissue engineering, Biomaterials 31 (3) (2010) 461–466.
[67] N. de Jonge, J. Foolen, M.C. Brugmans, S.H. Sontjens, F.P. Baaijens, C.V. Bouten, Degree of scaffold degradation influences collagen (re)orientation in engineered tissues, Tissue Eng. 20 (11–12) (2014) 1747–1757.
[68] R. Li, H. Liu, H. Huang, W. Bi, R. Yan, X. Tan, W. Wen, C. Wang, W. Song, Y. Zhang, F. Zhang, M. Hu, Chitosan conduit combined with hyaluronic acid prevent sciatic nerve scar in a rat model of peripheral nerve crush injury, Mol. Med. Rep. 17 (3) (2018) 4360–4368.
[69] J. Chedly, S. Soares, A. Montembault, Y. von Boxberg, M. Veron-Ravaille, C. Mouffle, M.N. Benassy, J. Taxi, L. David, F. Nothias, Physical chitosan microhydrogels as scaffolds for spinal cord injury restoration and axon regeneration, Biomaterials 138 (2017) 91–107.
[70] M.A. Gamiz-Gonzalez, D.M. Correia, S. Lanceros-Mendez, V. Sencadas, J.L. Gomez Ribelles, A. Vidaurre, Kinetic study of thermal degradation of chitosan as a function of deacetylation degree, Carbohydr. Polym. 167 (2017) 52–58.
[71] A. Sionkowska, M. Wisniewski, J. Skopinska, C.J. Kennedy, T.J. Wess, Molecular interactions in collagen and chitosan blends, Biomaterials 25 (5) (2004) 795–801.
[72] H. Cassimjee, P. Kumar, P. Ubanako, Y.E. Choonara, Genipin-crosslinked, proteosaccharide scaffolds for potential neural tissue engineering applications, Pharmaceutics 14 (2) (2022).
[73] L. Peruzzotti-Jametti, C.M. Willis, R. Hamel, G. Krzak, S. Pluchino, Metabolic control of smoldering neuroinflammation, Front. Immunol. 12 (2021) 705920.
[74] F.S. Mohammed, S.B. Omay, K.N. Sheth, J. Zhou, Nanoparticle-based drug delivery for the treatment of traumatic brain injury, Expet Opin. Drug Deliv. 20 (1) (2023) 55–73.
[75] N. Ghandy, A. Ebrahimzadeh-Bideskan, A. Gorji, S.S. Negah, Co-transplantation of novel Nano-SDF scaffold with human neural stem cells attenuates inflammatory responses and apoptosis in traumatic brain injury, Int. Immunopharm. 115 (2023) 109709.
[76] S. Jin, Y. Wang, X. Wu, Z. Li, L. Zhu, Y. Niu, Y. Zhou, Y. Liu, Young exosome bio-nanoparticles restore aging-impaired tendon stem/progenitor cell function and reparative capacity, Adv. Mater. 35 (18) (2023) e2211602.